Modeling Nanofiltration for Large Scale Desalination Applications

by

Yagnaseni Roy

B.Tech. Mechanical Engineering

SRM University, 2013

SUBMITTED TO THE DEPARTMENT OF MECHANICAL ENGINEERING IN PARTIAL FULMILLMENT OF THE REQUIREMENTS FOR THE DEGREE OF

MASTER OF SCIENCE
AT THE
MASSACHUSETTS INSTITUTE OF TECHNOLOGY
JUNE 2015

Signature of Author: Signature redacted

Department of Mechanical Engineering
May 7, 2015

Certified by: Signature redacted

John H. Lienhard V
Abdul Latif Jameel Professor
Thesis Supervisor

Accepted by: Signature redacted

David E. Hardt
Chairman, Committee on Graduate Students

Modeling Nanofiltration for Large Scale Desalination Applications

by

Yagnaseni Roy

Submitted to the Department of Mechanical Engineering
on May 14, 2015, in partial fulfillment of the
requirements for the degree of
Master of Science in Mechanical Engineering

Abstract

The Donnan Steric Pore Model with dielectric exclusion (DSPM-DE) is implemented over flat-sheet and spiral-wound leaves to develop a comprehensive model for nanofiltration modules. This model allows the user to gain insight into the physics of the nanofiltration process by allowing one to adjust and investigate effects of membrane charge, pore radius, and other membrane characteristics. The study shows how operating conditions such as feed flow rate and pressure affect the recovery ratio and solute rejection across the membrane. A comparison is made between the results for the flat-sheet and spiral-wound configurations. The comparison showed that for the spiral-wound leaf, the maximum values of transmembrane pressure, flux and velocity occur at the feed entrance (near the permeate exit), and the lowest value of these quantities are at the diametrically opposite corner. This is in contrast to the flat-sheet leaf, where all the quantities vary only in the feed flow direction. However it is found that the extent of variation of these quantities along the permeate flow direction in the spiral-wound membrane is negligibly small in most cases. Also, for identical geometries and operating conditions, the flat-sheet and spiral-wound configurations give similar results. Thus the computationally expensive and complex spiral-wound model can be replaced by the flat-sheet model for a variety of purposes. In addition, the model was utilized to predict the performance of a seawater nanofiltration system which has been validated with the data obtained from a large-scale seawater desalination plant, thereby establishing a reliable model for desalination using nanofiltration.

Thesis Supervisor: John H. Lienhard V
Title: Abdul Latif Jameel Professor

Acknowledgements

I would like to express my sincere gratitude to Professor John H. Lienhard V for giving me the opportunity to participate in research with a massive global impact, I feel proud to have played a part in addressing global water issues under his supervision. I thank him for his continuous support- every conversation with him seeded new and exciting ideas in my mind. He allowed me to pursue my interests in an unfettered manner, which has allowed me to enjoy my research and thus expand my knowledge and contribute to the field of desalination with excitement.

In the intense life-style that MIT has demanded of me, I have always been fortunate to have a loving family that has held my hand while crossing bumpy roads, even from thousands of miles away. I thank my parents for their constant help and involvement in my life. From helping me manage my paper-work to listening to me rant about problem sets, you have taken it all with a smile. I don't think I will ever be capable of managing my life without you.

I thank my lab-mates for everything I have learnt from them, for the constant feedback on my work which has always opened up new avenues of thought for me; the support in difficult situations and so much more. I'd like to say a special thanks to Leo, Greg and Jai for being my guiding stars! I also express my gratitude to Professor Mostafa Sharqawy for his constant help in my research and for providing excitement and creativity in the work we have done together.

Finally, the person who I constantly try to emulate, not only for the academic giant he is, but also his generosity and kindness, Professor Sarit K. Das. I thank him for taking me under his wing

and training me to be good enough to be at MIT. A major driving force in my life is to make him proud and meet up to his expectations from me.

I express my gratitude as well to the King Fahd University of Petroleum and Minerals in Dhahran, Saudi Arabia, for funding the research reported in this work through the Center for Clean Water and Clean Energy at MIT and KFUPM.

THIS PAGE IS INTENTIONALLY LEFT BLANK

Contents

THIS PAGE IS INTENTIONALLY LEFT BLANK

List of Figures

THIS PAGE IS INTENTIONALLY LEFT BLANK

List of tables

Nomenclature

A_k	porosity of membrane	
C	concentration	mol m^{-3}
C_X	membrane volumetric charge density	mol m^{-3}
dS	contact area between channel and membrane in each cell	m^2
D	solute diffusivity	m^2 s^{-1}
D_H	hydraulic diameter of feed channel	m
f	friction coefficient	
F	Faraday's constant	C eq^{-1}
i_v	Van 't Hoff coefficient	
h	channel height	m
j	solute flux	mol $m^{-2}s^{-1}$
J_w	solvent permeation flux	m s^{-1}
k	mass transfer coefficient in feed channel	m s^{-1}
K	hindrance factor	
l	distance along the feed channel	m
L	membrane length	m
L_{mix}	mixing length of spacer	m
$\dot{m}$	mass flow rate	mol
P	Pressure	Pa
ΔP_{net}	net driving pressure	Pa

ΔP_{loss}	hydraulic pressure loss along feed channel	Pa
Q	flow rate	$m^3 s^{-1}$
r_{pore}	pore radius of membrane	m
R	universal gas constant	$J mol^{-1} K^{-1}$
T	temperature	K
u	Velocity	$m s^{-1}$
W	membrane width	m
x	distance normal to membrane	m
Δx	membrane active layer thickness	m
z	valence of species	

Greek symbols

γ	activity coefficient	
ε_{pore}	pore dielectric constant	
ζ	Potential gradient at feed-membrane interface	$V m^{-1}$
η	mixing efficiency of spacer	
ν	kinematic viscosity	$m s^{-1}$
π	osmotic pressure	$N m^{-2}$
ρ	density	$kg m^{-3}$
Φ_i	steric partitioning factor	
Φ_B	Born solvation factor for partitioning	
ψ	membrane potential	V

Subscripts

c	convective
d	diffusive
D	Donnan potential
f	feed bulk
i	solute species
in	inlet
m	feed-membrane interface
out	outlet
p	permeate just outside the membrane
$pore$	inside pore
w	solvent
∞	Bulk

Dimensionless Parameters

Pe	Peclet number	$\frac{2h_f u_w}{D_\infty}$
Re	Reynolds number	$\frac{u_w D_H}{\nu}$
Sc	Schmidt number	$\frac{\nu}{D_\infty}$

Chapter 1

Motivation and Background

1.1 Significance of desalination and focus on Saudi Arabia

Desalination is the process of removing dissolved salts from water, thus producing fresh water from seawater or brackish water [1]. It is mainly used to produce potable water from saline water for domestic or municipal purposes, although its use for industrial applications is growing, especially in the oil & gas industry [1] [2]. It is a major source of fresh water for people mostly in arid regions where surface and ground water reserves are scanty.

In Saudi Arabia, 70% of the water used in homes and a large fraction of water used in industry comes from desalination [3]. As a result, desalination is a booming industry in the Kingdom, and it is the world's largest producer of desalinated water, with a total of 27 plants (as of 2014) [2] [3]. The Saline Water Conversion Company (SWCC) owned by the Saudi Arabian government is the world's largest desalination enterprise and as of 2008, it owned 30 desalination plants over Saudia Arabia and as of 2013, it had 3.3 million m^3/day installed capacity [2]. All plants owned by SWCC consist of Multi-Stage-Flash (MSF) and Reverse-Osmosis (RO) units. In 2006, the SWCC released a patent [2]on the use of Nanofiltration as a pretreatment for MSF and RO in various configurations, which proved capable of increasing top brine temperature to 125°C from earlier top limit of 120°C. Further studies have shown that in principle, it is possible to further increase this value to 160°C [4].

The major goal of the work presented here is to develop a model for the nanofiltration units used in desalination plants and test theoretical limits of performance of the composite system after

inclusion of the nanofiltration unit. The model will predict the rejection ratio of various seawater ions and recovery ratio of the nanofiltration unit for various flow conditions. It will provide insight into the mechanism of nanofiltration in various membranes produced by various vendors. Such a detailed model may also give scope for research in the development of new and improved membranes.

1.2 Significance and uniqueness of nanofiltration

Nanofiltration (NF) is a membrane-based water purification process with performance between that of reverse osmosis (RO) and ultrafiltration (UF) [5], [6]. The interplay of three exclusion mechanisms, the steric effects (size-based exclusion due to a 'sieving mechanism'), Donnan exclusion effects (due to the electrostatic interaction of the ions with the charge established on the membrane), and dielectric effects (due to the dissimilarity of the dielectric properties between the aqueous solution and the membrane pores) allow a great degree of variability in membrane selectivity [7], [8], [9]. The relative rejection of different solutes by nanofiltration membranes of different structure and chemical composition varies as a result of this interplay and therefore provides potential for a great degree of variability in rejection performance [6]. In general, nanofiltration shows high rejection of divalent and multivalent ions relative to monovalent ions [10], [11], [12]. It created a revolution in the world of separation technology, previously dominated by RO, due to its high water permeability and hence lower energy consumption in addition to its ion selectivity [6], [13]. In its early days, nanofiltration was utilized predominantly in the dairy and chemical industries applications [13]. In more recent years, it has been used in a variety of applications such as desalination [6] [12], wastewater treatment [14], diafiltration [15], petroleum fractionation [2], and treatment of mining water [16].

1.3 Need for a comprehensive model for large-scale nanofiltration systems

Many simulation and performance evaluation software packages are available for NF systems. Membrane projection software such as IMS, ROSA and other such software released by membrane manufacturers are effective when used within the provided guidelines, however they are subject to several limitations [17], [18]. Although these programs each perform similar calculations, their input requirements are different and each of them only evaluates designs using the modules manufactured by the specific company owning the software. Thus, for the user, choosing a design is a hectic procedure involving inputting the same data in different formats for the different programs [18]. The results from these packages are performance projections based on the manufacturer's performance specifications for a membrane element. Since the results from an individual element often do not match the nominal values, these packages are accurate only for systems with a large number of membrane elements, so that positive and negative deviations from nominal values cancel [17]. Furthermore, such programs do not give insight into the detailed mechanism of nanofiltration, and some may only use solution-diffusion models of transport through the membrane [17]. This prevents the user from gaining insight on the difference in performance of the various membranes. The intricacy of the mechanism of nanofiltration is thereby underplayed in such models.

1.4 Introduction to the DSPM-DE model for nanofiltration

The Donnan Steric Pore Model with Dielectric Exclusion (DSPM-DE) is a comprehensive model of the mechanism of nanofiltration. This model solves the Extended Nernst-Planck

equation (ENP) for each solute species through the membrane and uses boundary conditions at the membrane surfaces to account for the Donnan exclusion, dielectric exclusion, and steric exclusion effects. It is an improvement upon the original Donnan Steric Pore Model (DSPM) [5] [7] [15] [19], as it explains in detail the mechanism of dielectric exclusion, which is vital for the correct prediction of the rejection of multivalent ions by the nanofiltration membrane. This model has been well validated with lab-scale experiments [8]. In the current work, the dielectric exclusion mechanism based on the Born effect is considered. The Born effect accounts for the energy barrier for solvation inside the pores and hence decreased dielectric constant of the solvent [7] [20] [21]. According to the work of Bowen et al [7], this mechanism of dielectric exclusion is dominant over the other effect used to explain dielectric exclusion, involving image charges that develop at the interface of the bulk solution and membrane (as described by Bandini et al [9]), for most nanofiltration conditions. This is explained by the fact that the small pores in nanofiltration membranes cause the value of the dielectric constant of the solvent inside the membrane approach that of the membrane itself and moreover, the image charges are screened in electrolyte solutions due to the formation of electrical double layers [7]. The DSPM-DE model using the Born effect for dielectric exclusion has been well validated with lab-scale experiments [8].

Geraldes *et al.* [8] introduced the software 'Nanofiltran' that solves the discretized and linearized ENP equations. Nanofiltran is a robust and comprehensive software that considers the non-ideality of solutions and the concentration polarization effect at the feed-side of the membrane. However, it models a 'small patch' of membrane and does not account for the streamwise distribution of various quantities, namely flow parameters such as cross-flow

velocities, solute concentrations, and transmembrane flux as well as solute rejection profiles along a large membrane leaf. Thus 'Nanofiltran' cannot be used to describe large membranes that are used in large-scale nanofiltration units.

1.5 Motivation behind this work

Hitherto, to the best knowledge of the authors, a comprehensive model of a spiral-wound module of nanofiltration that accounts for the detailed mechanism of nanofiltration has not been introduced. Schwinge *et al.* [18] showed a detailed analysis of spiral wound membranes and the spatial distribution of quantities such as transmembrane flux, transmembrane pressure, feed concentration, and crossflow velocity along the membrane. This study, however, is general and can be applied to reverse osmosis, nanofiltration, ultrafiltration, or microfiltration membranes. A complete study of nanofiltration membranes demands attention not only to the general features of the membrane, but also to its unique separation capability and mechanism. A comprehensive study of nanofiltration cannot be done by considering only the diffusive mechanism of solute transport though the membrane, as in reverse osmosis, or only the convective mechanism of solute transport as in ultrafiltration/microfiltration. Rather, it is a combination of the diffusive transport, electro-migration and convective transport through narrow pores, therefore requiring use of the Extended Nernst-Planck equation, modified by the hindered transport theory [7], [8], [9].

The NF model introduced in the present work is based on the DSPM-DE model, applied over a flat-sheet and spiral-wound leaf. The results from the individual leaves can be easily treated as if in a parallel connection to depict a spiral-wound element, which may in turn be put into a train

of spiral-wound elements that exist in series within a pressure vessel. The DSPM-DE model allows the user to experiment with the many control parameters and therefore test different existing membranes, as well as predict the performance of membranes with varied properties. The user can make use of several degrees of freedom in the definition of the membrane, namely the membrane pore radius, membrane effective thickness, membrane charge, pore dielectric constant and, membrane dimensions. It is also possible to test the behavior of individual leaves or an individual element for different feed flow rates, compositions, and transmembrane pressures. Various feed water properties, such as pH levels and temperature can be incorporated into the model by characterizing the membrane and subsequently using these parameters in the model [19].

Another important aim of this work is to provide results for each constituent ion of seawater from its nanofiltration modeling. Most commonly, seawater is modeled by a sodium-chloride solution at a concentration similar to that of seawater [22]. While this is a reasonable approximation for seawater [23] [24], it does not give any information about the permeate concentrations of the many individual ions in seawater. Thus, it fails to provide essential information regarding concentration of scale-causing ions such as magnesium, calcium, sulphate and carbonate ions that enter thermal desalination processes for which nanofiltration is used as a pretreatment [4].

The use of nanofiltration as a pretreatment stage in thermal desalination processes, namely, Multi-Stage Flash (MSF) and Multi-Effect-Distillation (MED) seawater desalination plants, in order to increase the top brine temperature (TBT), has been a subject of interest and study by several researchers [16], [4], [25], [26]. Nanofiltration efficiently removes scale-causing ions such as calcium, magnesium, sulphate and carbonate ions and hence adds potential to increase

the top brine temperature (TBT) in an MSF or MED plant. In reference [4], the Saline Water Conversion Corporation, Research and Development Center (SWCC-RDC) demonstrated that the addition of a nanofiltration unit as pretreatment to MSF was found to be successful in the removal of turbidity, residual bacteria, and scale forming constituents. Moreover, it resulted in lowering of the seawater total dissolved solids (TDS), and enabled increasing TBT up to 160°C [4]. Consequently, it reduced the thermal energy input and decreased the antiscalant additives, as evident from experimental results of a pilot plant. Several experimental efforts have been made on nanofiltration of seawater, both at lab scale as well as in desalination plants [26], [27], [28]. However, the aim of this work is to provide a useful model to reduce the number of experiments required for such studies.

In summary, this work aims at introducing a comprehensive model for flat-sheet and spiral-wound nanofiltration membranes and evaluates their performance for the seawater desalination application. A model is introduced for analyzing commercially used nanofiltration elements that allows the user to understand the mechanism of filtration and provides the flexibility to simulate a wide range of membrane types by adjusting the various key parameters that characterize the membrane. Further, a detailed analysis of seawater nanofiltration using this model is described.

THIS PAGE IS INTENTIONALLY LEFT BLANK

Chapter 2

Mathematical Model

The model presented in this work is an integrated version of the previously developed DSPM-DE model [8]. In this work, the elemental equations of that model are 'threaded together' to simulate the transport over a large membrane leaf with locally varying conditions. The large membrane leaf is divided into cells and the DSPM-DE model equations are applied by moving from one cell to another while accounting for the mass conservation of each solute species and of the solvent. In addition, the hydraulic pressure losses along the feed flow direction in the feed channel are considered. Figure 2-1 and 2-2 are schematic diagrams of the flat-sheet membrane leaf and the spiral-wound membrane leaf configurations respectively.

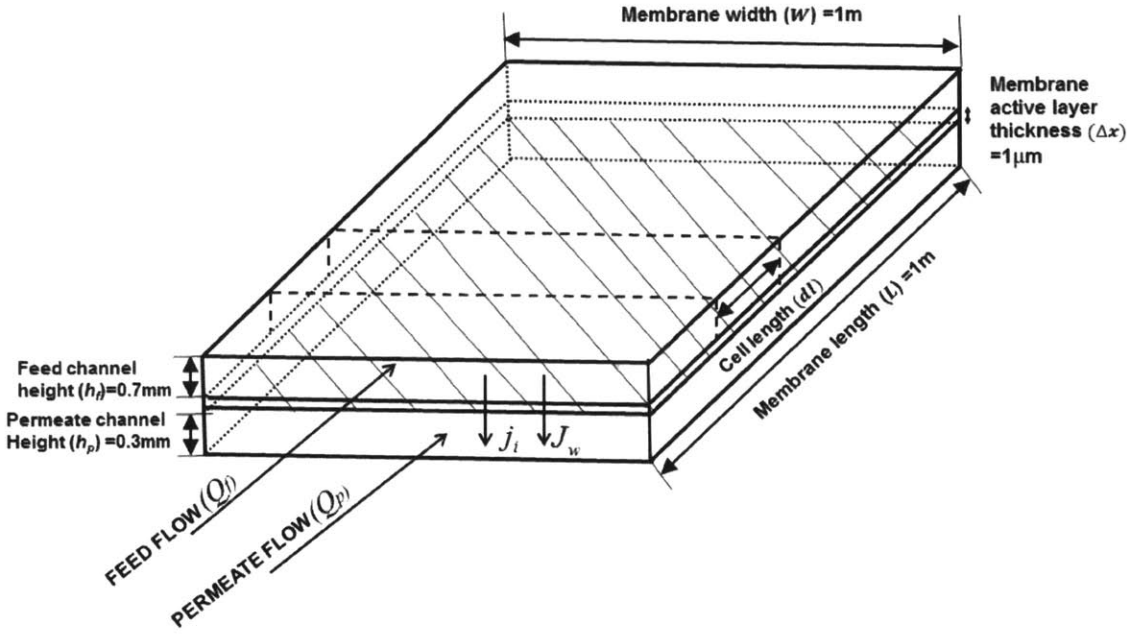

Fig. 2-1 Schematic diagram of flat-sheet membrane.

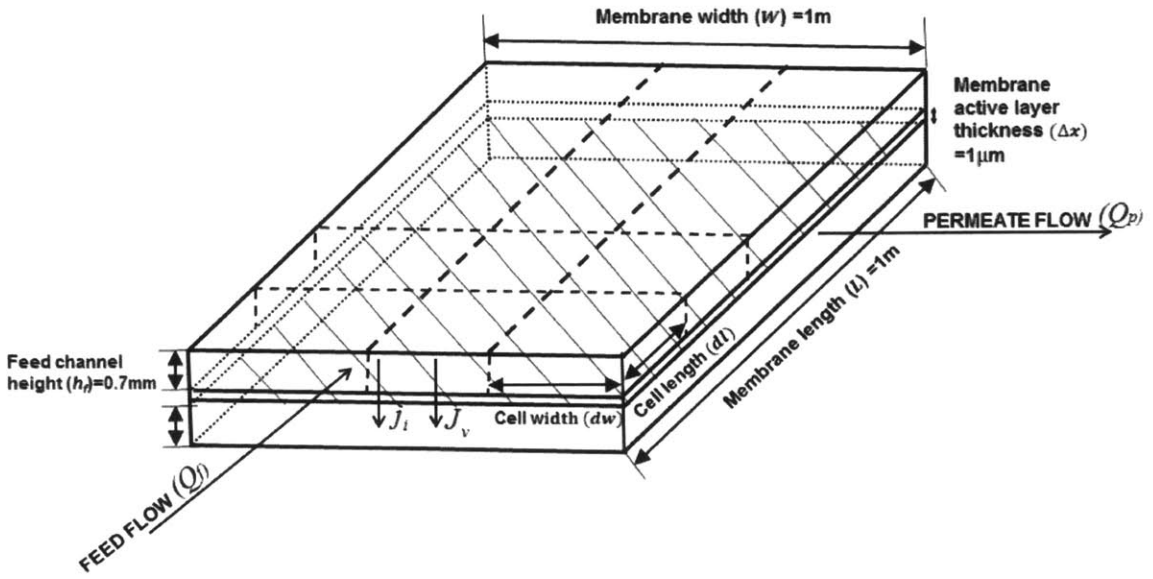

Fig. 2-2 Schematic diagram of spiral-wound membrane.

The two configurations differ by the flow arrangement. Figure 2-1 shows the flat-sheet membrane configuration with the feed and permeate flows in their respective channels, flowing parallel to one-another. The membrane leaf has a width W and a length L along the feed flow direction. As shown, the cells have a width equal to that of the membrane leaf and they split the length of the membrane into several segments. Figure 2-2 shows an unwound spiral-wound membrane leaf. In this configuration, the feed and permeate flow perpendicular to each other in their respective channels. Therefore, in order to capture the variation of the flow parameters and the rejection performance of the membrane in both the longitudinal and transverse directions, the cells are square elements that split both the width and length of the membrane into segments. Grid independence studies of the present work have showed that beyond 100 cells (in the feed flow direction for the flat-sheet case and 100 cells each in the feed and permeate flow directions

in the spiral-wound case), the computational results vary by less than 1%. Therefore, 100 cells were taken for all cases in the present work.

2.1 Governing Equations

The Extended Nernst-Planck equation (ENP) describes the transfer of ions under the influence of concentration gradient, electric field, and inertia forces. For each solute *'i'* transferring through the membrane pores, the ENP equation is given by Eq. (1).

$$j_{i,pore} = -D_{i,pore}\frac{dC_{i,pore}}{dx} - \frac{z_i C_{i,pore} D_{i,pore}}{RT} F \frac{d\psi}{dx} + K_{i,c} C_{i,pore} u_{i,pore} \qquad (1)$$

where $j_{i,pore}$ is the flux of the species *'i'* inside a pore, the first term on the right represents the transport due to diffusion (concentration gradient), the second term represents the transport due to electric field (potential gradient), and the last term represents the transport due to convective forces. Due to the extremely small pore sizes in nanofiltration membranes, the diffusive and convective transport of the solute are 'hindered'. Thus, the ENP has been modified by the hindered transport theory [29] [30] through introduction of the coefficients $K_{i,c}, K_{i,d}$ which give a measure of the 'lag' of a spherical solute moving inside a cylindrical pore and the enhanced drag experienced by the solute respectively. Both these coefficients are functions of the ratio of solute radius to pore radius [7].

The diffusivity (diffusion coefficient) of the solute inside the pore is related to the diffusivity of the solute in the bulk solution as given by Eq. (2):

$$D_{i,pore} = K_{i,d} D_{i,\infty} \tag{2}$$

The equilibrium boundary condition at the membrane-feed solution interface due to the combination of the steric, Donnan, and dielectric effects is given by

$$\frac{\gamma_{i,pore} C_{i,pore}}{\gamma_{i,m} C_{i,m}} = \Phi_i \Phi_B \exp\left(- \frac{z_i F}{RT} \Delta\psi_D \right)\Bigg|_{in} \tag{3}$$

It is to be noted that $C_{i,pore}$ in equation (3) is the solute concentration just within the pore 'entrance'. This is important because the solute concentration varies along the pore. $C_{i,m}$ is the feed concentration at the membrane-feed solution interface. $\gamma_{i,pore}, \gamma_{i,m}$ are solute activity coefficients just within the pore entrance and at the membrane and feed solution interface respectively; Φ_i, Φ_B are the steric partitioning factor and solvation energy contribution to partitioning respectively, and $\Delta\Psi_D$ is the Donnan potential difference across the membrane.

Similarly, the equilibrium boundary condition at the membrane-permeate solution interface is given by

$$\frac{\gamma_{i,pore} C_{i,pore}}{\gamma_{i,p} C_{i,p}} = \Phi_i \Phi_B \exp\left(- \frac{z_i F}{RT} \Delta\psi_D \right)\Bigg|_{out} \tag{4}$$

In Eq. (4), the quantities with subscript '*pore*' are at the exit of the pore, just within the membrane and the quantities with subscript '*p*' represent values in the permeate solution just outside the membrane [8].

The ENP equations (given by Eq. (1)) and the relevant boundary conditions (given by Eq. (3) and Eq. (4)) are solved numerically for each solute in each cell. Equations (3) and (4) state that the concentration just within the membrane versus that at the contact surface of the membrane and the feed/permeate solution is governed by the steric, Donnan, and dielectric exclusion effects. It is assumed that the membrane element is working under steady state condition and both solute and solvent mass flow rate are conserved in travelling from one cell to the next. Since at steady state, the molar flux of the solute is independent of its position inside the pore, the following relation is valid [8]:

$$j_{i,pore} = C_{i,p} J_w \tag{5}$$

where $C_{i,p}$ is the permeate concentration just outside the membrane at the permeate side [8].

The mass balance of each solute species *'i'* in the feed channel is given by Eq. (6).

$$d\dot{m}_{i,f} = -C_{i,p} J_w dS \tag{6}$$

where $m_{in,f}$ and $m_{out,f}$ are the mass of the solute *'i'* entering and exiting the current cell respectively.

Similarly, the mass balance of each solute species *'i'* in the permeate channel is given by Eq. (7).

$$d\dot{m}_{i,p} = C_{i,p} J_w dS \tag{7}$$

On the other hand, the solvent mass balance on the feed side is given by Eq. (8).

$$dQ_f = -J_w dS \tag{8}$$

Similarly, the solvent mass balance on permeate side is given by Eq. (9).

$$dQ_p = J_w dS \tag{9}$$

The model equations described above (Eq. 1 to 9) are discretized by the finite forward difference method and solved numerically using MATLAB (version R2013b). After solving the model equations and getting the velocity and concentration fields, the hydraulic pressure loss along the feed flow direction is determined by the friction factor. The correlation of the friction coefficient in the feed channel of FilmTec membrane element is taken from [31] which fit with experimental data.

$$f = \frac{6.23}{\mathrm{Re}^{0.3}} \tag{10}$$

Accordingly, the pressure drop along the feed channel in the feed flow direction is given by Eq. (11).

$$\Delta P_{loss} = -\frac{f}{2}\frac{l}{D_H}\rho_w u_w{}^2 \tag{11}$$

where l is the length along the feed channel in the feed flow direction, u_w is the bulk velocity of flow at that location, and D_H is the hydraulic diameter of the feed channel. In a single leaf, the permeate flow rate is low compared to the feed flow rate even at high recovery ratios. Consequently, the permeate Reynolds number is also low and there is no significant hydraulic

pressure loss in the permeate channel. Therefore, the hydraulic pressure drop in the permeate channel was not included and the permeate channel was considered to be uniformly at atmospheric pressure.

For the mass transfer coefficient, the expression given by [32] and [33] for spiral wound membranes (which includes the effect of spacers) was used as given by Eq. (12)

$$k_i = 0.753\left(\frac{\eta}{2-\eta}\right)^{1/2}\left(\frac{D_{i,\infty}}{h_f}\right)Sc^{-1/6}\left(\frac{Pe_i}{h_f L_{mix}}\right)^{1/2} \tag{12}$$

where: η is the mixing efficiency of spacer; L_{mix} is the mixing length of the spacer; h_f is the feed channel height; Pe_i is the Peclet number in the channel given by $Pe_i = \frac{2h_f u_w}{D_{i,\infty}}$; and Sc_i is the Schmidt number for each solute species, given by $Sc_i = \frac{\nu}{D_{i,\infty}}$.

Concentration polarization on the feed side is considered by applying a mass balance at the interface between the feed solution and the membrane, as given by Eq. (13) [8]. However, the permeate side concentration polarization is neglected, which is a reasonable assumption for pressure-driven membrane processes such as nanofiltration and reverse osmosis [34], [35], [36].

$$j_i = -k_i(C_{i,m} - C_{i,f}) + J_w C_{i,m} - z_i C_{i,m} D_{i,\infty}\frac{F}{RT}\xi \tag{13}$$

where ξ is the electrical potential gradient at the feed-membrane interface in the continuum phase [8].

The transmembrane osmotic pressure is calculated by the Van 't Hoff equation in any cell

$$\Delta\pi = i_v RT(C_m - C_p) \tag{14}$$

where C_m is the salt concentration at the feed-membrane interface, i_v is the Van 't Hoff coefficient, R is the universal gas constant, and T is the absolute temperature.

Finally, the transmembrane solvent flux is calculated from Eq. (15) as shown below:

$$J_w = \Delta P_{net}\left(\frac{r_{pore}^2}{8\nu\rho_w\left(\frac{\Delta x}{A_k}\right)}\right) = ((P_f - P_p) - \Delta\pi)\left(\frac{r_{pore}^2}{8\nu\rho_w\left(\frac{\Delta x}{A_k}\right)}\right) \tag{15}$$

For our simulations, the NF270 membrane manufactured by Dow and FilmTec was considered. Several authors have investigated this membrane and reported experimental results for the rejection ratio at different fluxes. By fitting the experimental data to the DSPM-DE model, it is found that the membrane has an average pore radius of 0.43 nm and an active layer thickness to porosity ratio of (Δx/A$_k$) about 1μm [20], [37]. In addition, , the pore dielectric constant is 42.2 from fitting with experiments with sodium-chloride [20]. With the exception of the fitting from magnesium-sulphate experimental data, the NF 270 membrane is found to have a pore dielectric constant close to 40 after fitting with several other solutes [20].

In fact, it is seen that for membrane characterization purposes, among the four parameters required to characterize a nanofiltration membrane, namely pore radius (r_{pore}), ratio of the membrane active layer thickness to porosity ($\Delta x / A_k$), pore dielectric constant (ε_{pore}), and

membrane volumetric charge density (C_X), the first three parameters can be assumed unique for a given membrane without much error. These three parameters do not change with the solute concentration in the feed, solution pH or the nature of the solute. However, when any of these parameters are fitted with respect to data from different solutes, their fitted values may vary slightly [7], [20]. These values are numerically very close and therefore, an average value is usually taken [20].

The remaining parameter, the membrane volumetric charge density (C_X), depends on the solute and solvent nature, the solute concentration, and the pH of the solution [7], [20], [21]. Therefore, this parameter must be carefully determined for each case investigated. Taking the values of pore radius, active layer thickness to porosity ratio, and the pore dielectric constant for NF270 as mentioned previously, an effective membrane volumetric charge density was fitted to data taken from [38] (see Table 1.2 in this reference). In this regard, the flow parameters in the present model were adjusted similar to those ones in [38] and the rejection ratio and recovery ratio from the model are then matched (with those measured in [38]) by adjusting the membrane charge in the model. For instance, at a feed solution of 2000 ppm sodium-chloride, in order to achieve a recovery ratio of about 10% and mean rejection of sodium-chloride of 80%, an effective membrane charge density of C_X=-45mol/m^3 was calculated. Comparing this value with values fitted by other researchers for FilmTec membranes, it was found that this value is within reasonable limits for the DSPM-DE model [21]. Therefore, a uniform average membrane charge across the entire membrane is assumed in our model using the calibration step discussed above. It is important to note that in reference [21], the variation of the membrane charge density with solute concentration is investigated for NF250 and NF300, showing that the membrane charge density increases linearly with the concentration of sodium-chloride and consequently, the

rejection ratio increases monotonically. This is verified by [7] where they show the same trend for Desal-DK membrane for both sodium-chloride and magnesium chloride solutions. Further, from our simulations, it is observed that with increasing membrane charge, each of the quantities such as rententate concentration, permeate concentration, rejection ratio, recovery ratio, transmembrane flux and feed flow rates either increase or decrease monotonically. Therefore, if variation of membrane charge were included in the simulation, it would fine-tune the results for each of these quantities, but would not affect the trends observed in the study conducted. The values used to characterize the NF-270 membrane for this case are given in Table 1.

For the spiral-wound membrane configuration, the conservation equations are modified to allow for variation of various flow parameters and concentration profiles both in the direction of flow of feed as well as in the perpendicular direction, due to the cross-flow of the permeate stream. According to [39], for a spiral-wound leaf, the height of the feed channel is very small which allows the curvature of the channel to be ignored. Thus, the feed channel in a spiral-wound leaf can be modeled as a thin rectangular duct with a height range of 0.5 – 2 mm. In the present model, the feed channel height was fixed at 0.7 mm, the permeate channel height is of 0.3 mm, and each leaf has a dimension of 1m × 1m, which are commonly used values in commercial spiral-wound membranes [31]. For the flat-sheet membrane, we assumed the same dimensions as for the spiral-wound module in order to make their comparison easier. Since the aim of our study is to investigate the effect of different flow parameters on the nanofiltration performance in the two configurations, it is necessary for the two modules to be similar in structure, thereby allowing us to study the difference in performance due to their different flow configurations.

2.2 Model Validation

Referring to the schematic diagrams shown in Fig. 2-1 and Fig 2-2, validation of our model is performed by comparing the performance results at various operating limits. When the width and length of the leaf are reduced to a few centimeters, the model results from both the flat-sheet and spiral-wound configurations were compared with the experimental measurements conducted at the lab scale using test cells. In this manner, the large membrane leaf was geometrically reduced to a 'small patch' of membrane or a zero dimensional (0-D) model. At this limit, there is negligible variation of quantities such as feed concentration and rejection ratio along the length and width of the membrane. Excellent agreement with the experimental data presented by [20] is obtained. In this reference, experiments are performed using a cross-flow test cell manufactured by GE Osmonics, using NF270 and NF99HF membranes at their respective isoelectric points. The comparison of the simulation results at this limit and the experimental data is shown in Fig. 2-3. In this limit, since the flat-sheet and spiral-wound modules give very similar results, only one set of simulation data is presented for validation.

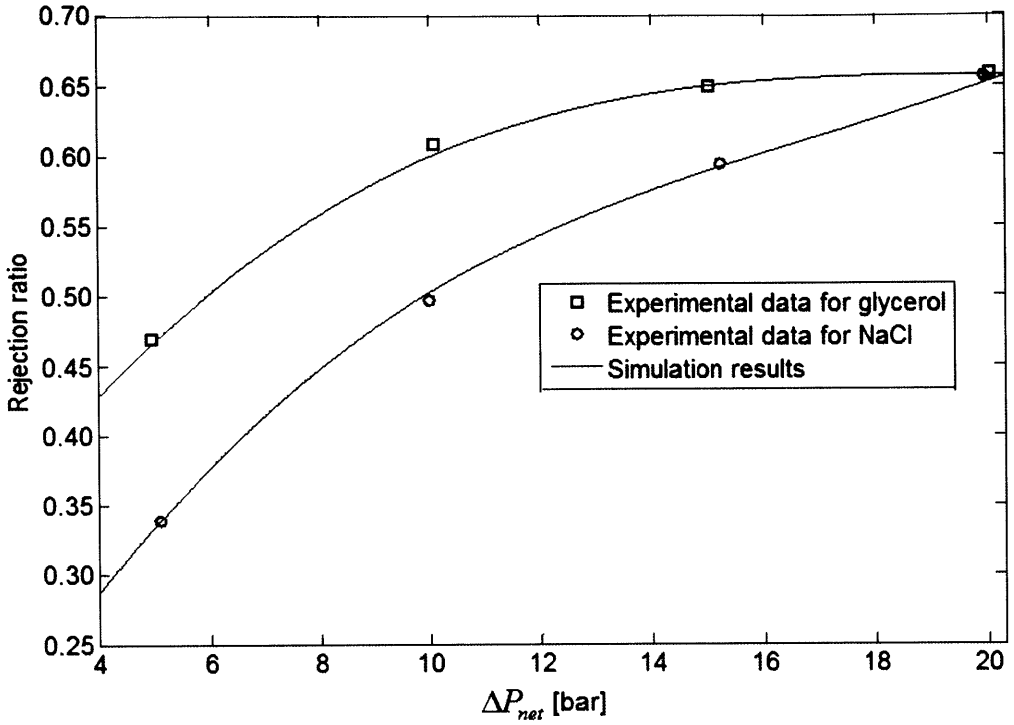

Fig. 2-3 Comparison between the present model results and lab-scale experiments using stirred-cell sized membranes [20].

Another test was conducted on the model to ascertain that the formulation for fluid flow was accurate. The aim is to see if in the limit of very small transmembrane flux, the feed channel matches the hydraulic behavior of a duct of similar dimensions. The dimensions of the feed channel were changed to a duct of 0.6 m width, 10 m length, and 0.3 m height. The pore radius was reduced to 0.23 nm in order to minimize the flux through the membrane and hence mimic the ordinary duct closely. The transmembrane flux was thus reduced to 13 L/m^2-h and the recovery ratio was 0.0042%, signifying that very little solvent flowed through the membrane. It

is assumed that the duct carries water at 10 °C at a flow rate of 30 m^3/min. The friction factor was found to be 0.014 at the corresponding Reynolds number and the hydraulic loss was calculated to be 1.35 kPa (0.1377 m). Our model for this duct gives a value of 1.32 kPa (0.1353 m) hydraulic loss on both the flat-sheet and spiral-wound modules, which is less than 1.7% deviation from the value of the normal duct.

Another validation was conducted with respect to the data provided in Dow technical manual which describes the experimental performance of NF270 membrane under standard test conditions. For the given set of input conditions, the simulation results of the NF270 membrane from the present model are compared with the data provided by Dow [38] using the membrane characteristics shown in Table 2.1. Our model predicts a recovery ratio of 10% and a mean rejection ratio of 80% for a feed solution of 2000 ppm sodium-chloride as tested and reported in the Dow's manual [38]. These values are in exact agreement with the experimental values reported in Dow manual for the recovery ratio and rejection ratio respectively.

Table 2.1 Values of membrane characterization parameters

Parameter	Value
r_{pore}	0.43 nm
$\Delta x / A_k$	1 μm
ε_{pore}	43.3
C_X	-45 mol/m^3

Furthermore, from our model, the characteristic features of the spiral-wound membranes can be observed. These features are in good agreement with the observations found from the detailed modeling study of spiral-wound leaves presented in [18].

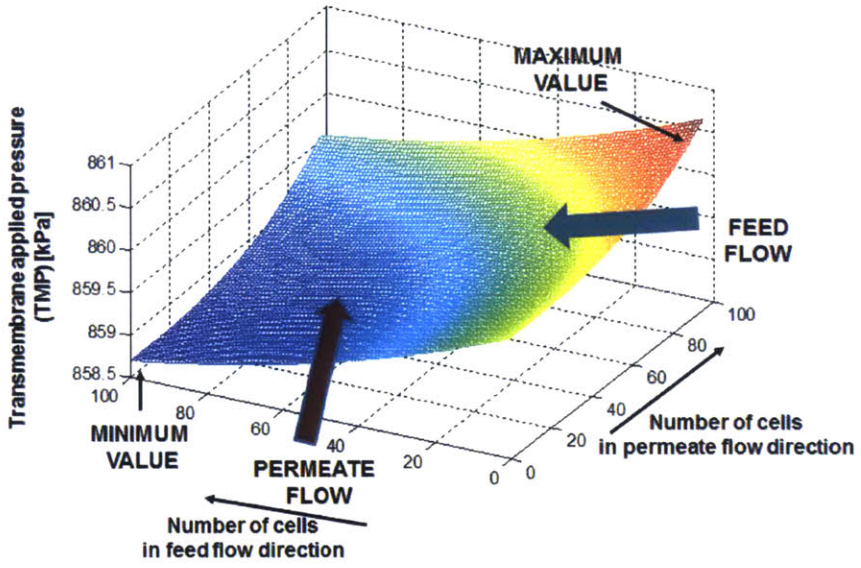

Fig. 2-4 Variation of the trans-membrane pressure over the area of the spiral-wound membrane at feed flow rate of 144 L/h and inlet feed pressure of 1 MPa

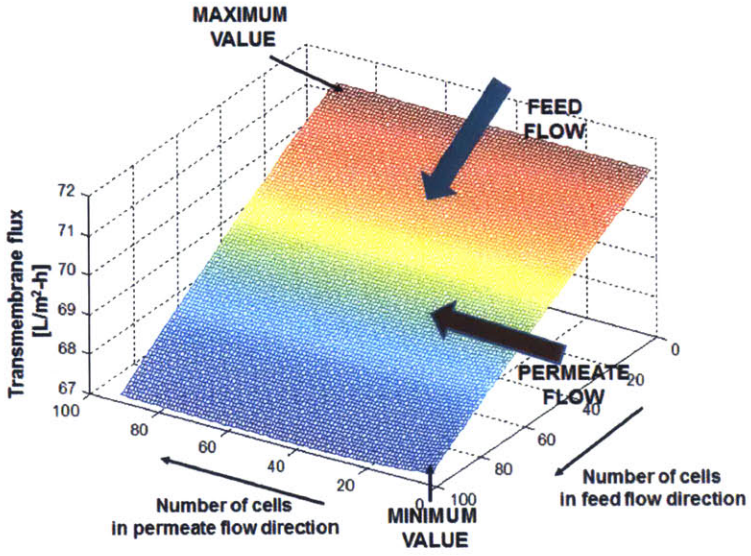

Fig. 2-5 Variation of the trans-membrane flux over the area of the spiral-wound membrane at feed flow rate of 144 L/h and inlet feed pressure of 1 MPa.

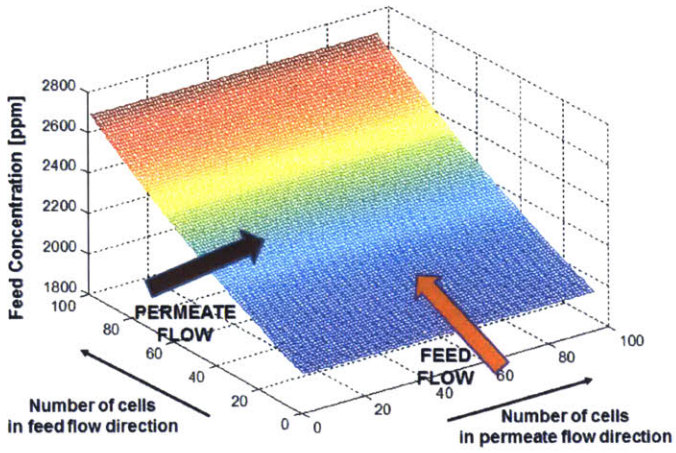

Fig. 2-6 Variation of the feed concentration over the area of the spiral-wound membrane at feed flow rate of 144 L/h and inlet feed pressure of 1 MPa

Figure 2-4, 2-5, and 2-6 show the variations of the trans-membrane pressure (TMP), trans-membrane flux, and feed concentration on the membrane surface respectively. This simulation is conducted at a feed pressure of 1 MPa, feed flow rate of 144 L/h, and an inlet sodium-chloride feed concentration of 2000ppm. It is shown that the maximum values of trans-membrane pressure, trans-membrane flux, and velocity occur at the feed entrance (near the permeate exit side), where the salt concentration is the lowest [18]. This trend is the most prominent for the trans-membrane pressure and to a lesser extent for trans-membrane flux as given in [18]. In addition, at the diagonally opposite corner of the membrane, at the feed exit (near the permeate entrance) the trans-membrane pressure, trans-membrane flux, and velocity show minimum values where the feed salt concentration is the highest. Figures 2-4, 2-5 and 2-6 illustrate the important characteristic traits of a spiral-wound membrane using our model. Exact values of concentration and other quantities at different points on the membrane surface for a nanofiltration spiral-wound membrane were not found in literature which indicates the importance of the present 2D model.

THIS PAGE IS INTENTIONALLY LEFT BLANK

Chapter 3

Results and Discussion

3.1 Effect of flow conditions in flat-sheet model

In this section, parametric studies are conducted in order to understand the operation of a nanofiltration module and the effect of different flow parameters on its performance. The results presented here are for a 2000 ppm solution of sodium-chloride at 25 °C. Firstly, a single leaf of a flat-sheet membrane as shown in Fig. 2-1 is considered. The variation of feed and permeate Reynolds numbers along the membrane in the direction of feed flow are fundamental in explaining several other trends, so they are investigated first.

The feed Reynolds number decreases along the membrane, since the average bulk flow velocity decreases along the membrane. This results from the decrease in the feed flow volume due to permeation of solution to the permeate side through the membrane. At higher feed flow rates, the feed Reynolds number is greater, as there is greater flow through fixed channel dimensions, causing average bulk flow velocity to be higher. The permeate Reynolds number increases along the membrane, due to the increase in permeate flow rate as a result of the flux entering through the membrane. According to Vitor *et al.* [39] for rectangular channels, the transition between laminar and turbulent flow occurs at a Reynolds number between 150 and 300 in the presence of spacers. In our work, operation over a large range of feed Reynolds number is shown. For instance, at the minimum feed flow rate of 60 L/h per leaf, the feed Reynolds number at the inlet is 50, while for the maximum feed flowrate of 1000 L/h per leaf, the Reynolds number at the inlet is 600.

Figure 3-1 shows the variation of the feed pressure along the membrane length. The feed pressure decreases along the membrane in the feed flow direction due to hydraulic losses. At higher flow rates and hence higher feed Reynolds numbers, the hydraulic losses are greater due to greater average velocity in the feed channel. Thus, the pressure variation lines slope down at greater angles for greater flow rates. On the other hand, the permeate Reynolds number is maximum at the permeate exit, since the flux permeated through the entire membrane adds up at that point. However, the maximum value of permeate Reynolds number does not exceed 20 at any of the feed flow rates investigated. Thus, due to the very low permeate Reynolds numbers, the hydraulic losses are insignificant and permeate hydraulic pressure remains essentially uniform along the flow direction. Therefore, the trans-membrane hydraulic pressure (TMP) is essentially a sole function of the feed pressure.

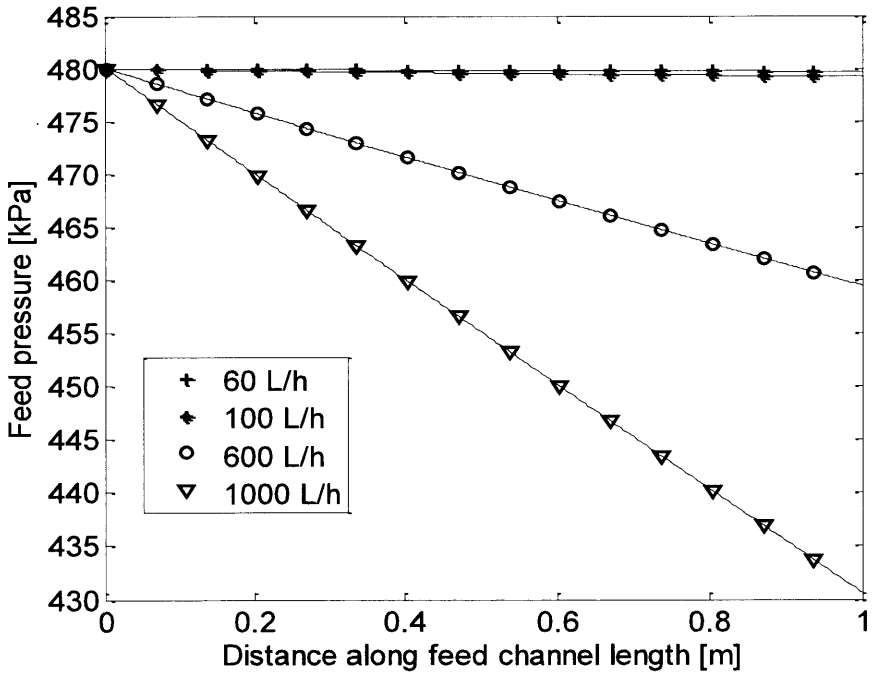

Fig. 3-1 Feed pressure variation along the feed flow direction at 480 kPa inlet feed pressure and different feed flow rates.

The variation of the solute mass transfer coefficient in the feed channel with respect to feed flow rate is essential in describing the concentration polarization at different flow rates. Its value is proportional to the feed Reynolds number values, and thus at higher Reynolds numbers, there is higher convective mass transfer from the membrane surface to the feed bulk solution, resulting in lower concentration polarization. Figure 3-2 and 3-3 show the variations of the bulk feed concentration at different feed flow rates and feed inlet pressures respectively.

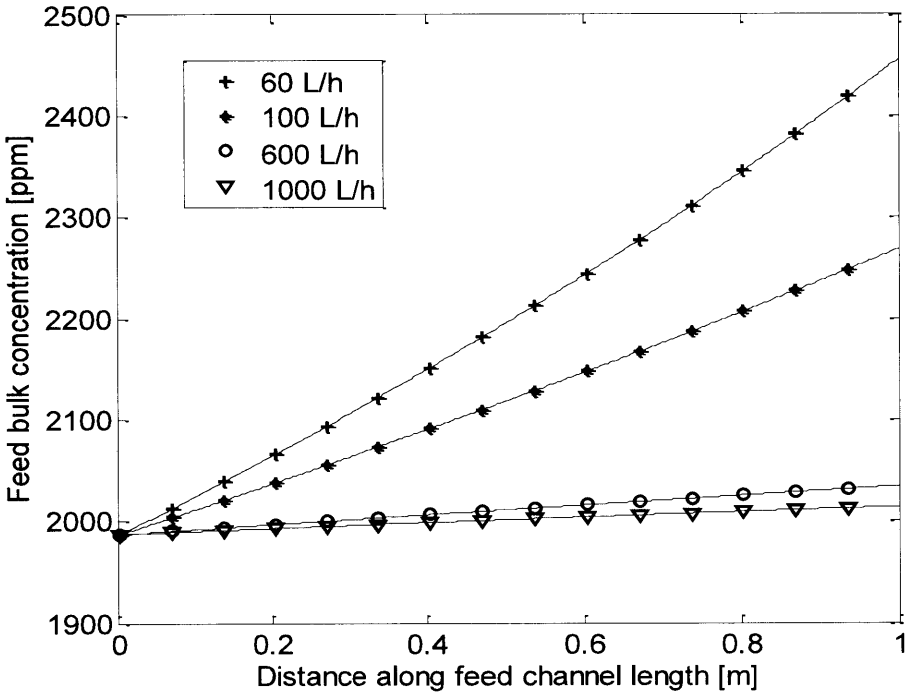

Fig. 3-2 Variation of feed bulk concentration along feed flow direction at 480 kPa inlet feed pressure and different feed flow rates.

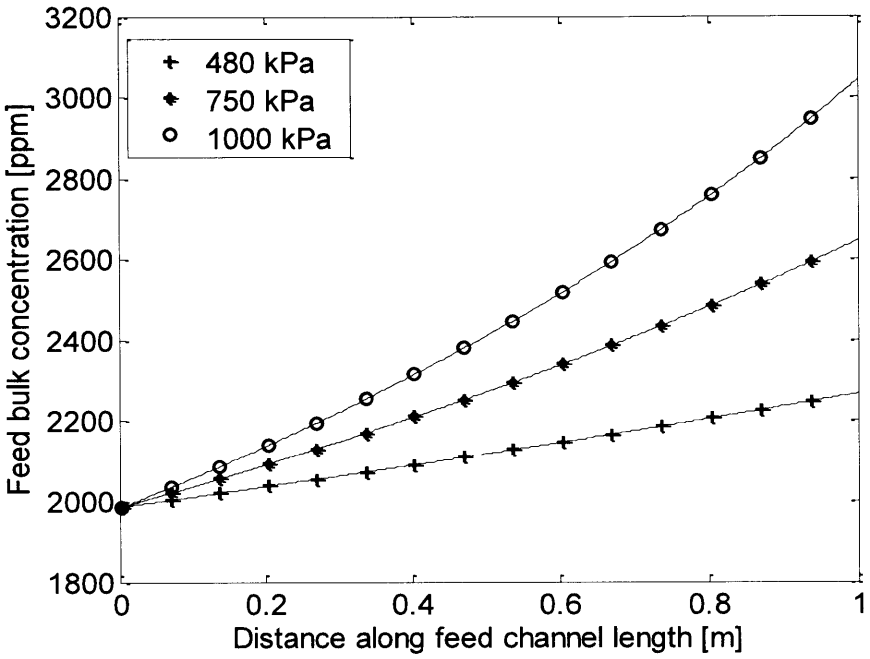

Fig. 3-3 Variation of feed bulk concentration along feed flow direction at 100 L/h flow rate and different feed inlet pressures.

Figure 3-4 shows the concentration at the membrane surface at different feed flow rates and feed pressures. It is noticed in Figs 3-2 to 3-4 that at the lowest feed flow rates there is a steep increase of the feed concentration and the concentration at the membrane surface in the flow direction. This is because the Reynolds number decreases to a small value along the feed channel as a result of a low mass flow rate, which also leads to a low mass transfer coefficient, so there is greater concentration polarization. Since at higher values of Reynolds number, there is the combined effect of the higher bulk solute mass flow rate in the feed channel together with the increased convection from the membrane to the bulk of the feed (lower concentration

polarization), very little solute enters the permeate channels. This is evident from Fig. 3-5, which clearly shows that the permeate concentration decreases at higher feed flow rates. Due to the inverse argument, the permeate concentration increases along the membrane due to the decreasing feed Reynolds numbers.

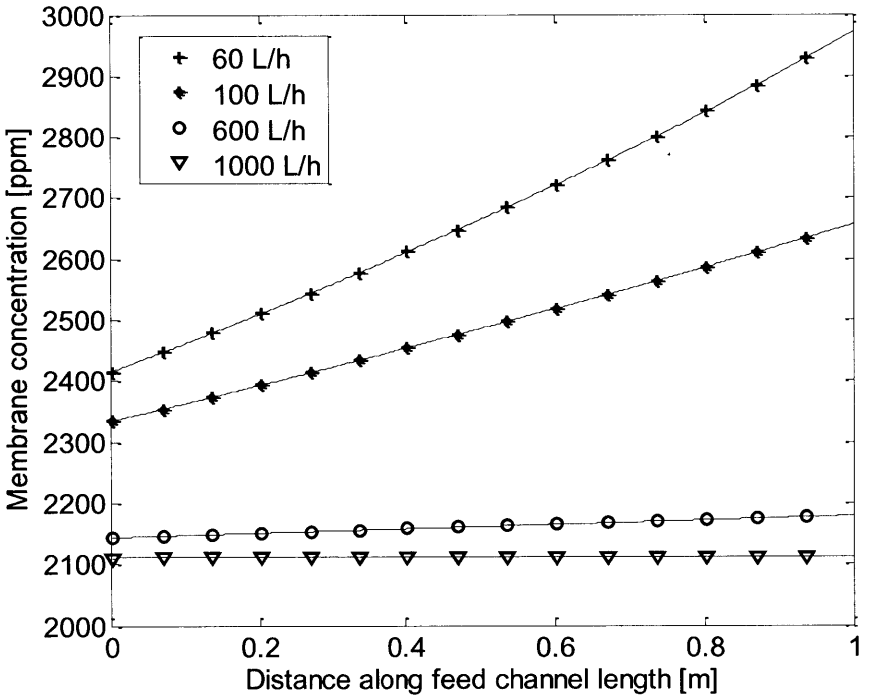

Fig. 3-4 Variation of the feed concentration at membrane surface on feed side along the feed flow direction at 480 kPa inlet feed pressure and different feed flow rates.

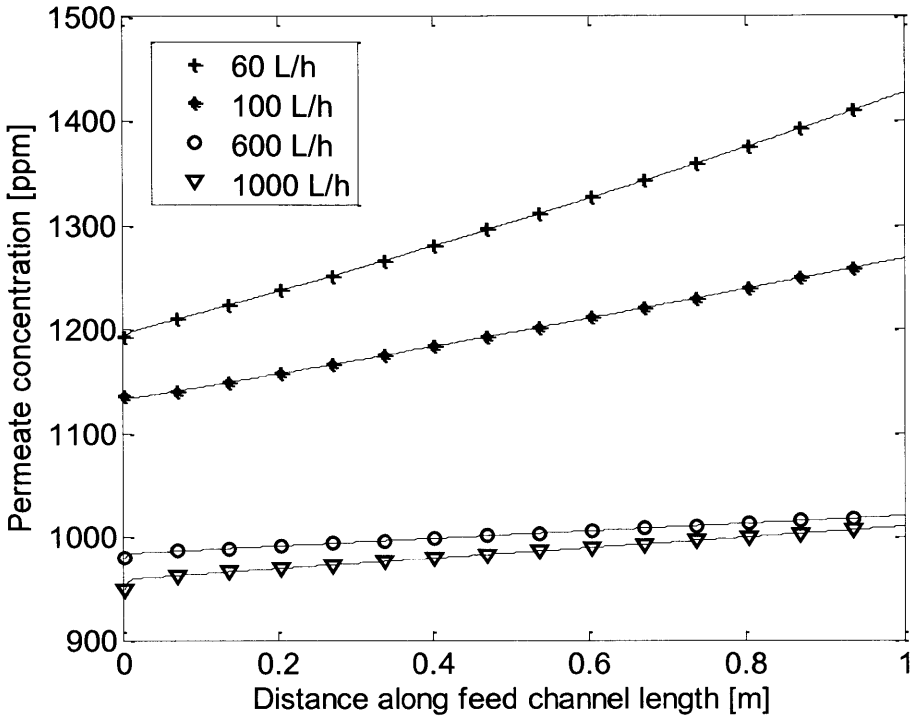

Fig. 3-5 Variation of permeate concentration along feed flow direction at 480 kPa inlet feed pressure and different feed flow rates.

The trans-membrane osmotic pressure, as given by Eq. (14) follows the trend of the membrane concentration, since the variation of permeate concentration along the channel is relatively small. For a given feed pressure, the net driving pressure, defined in Eq. (15) as $\Delta P_{net} = ((P_f - P_p) - \Delta\pi)$, first increases with the flow rate and then decreases (see Fig. 3-6). This is because initially, at lower feed flow rates, the feed pressure dominates over the trans-membrane osmotic pressure, resulting in high net driving pressure. However, with increasing feed flow rates, the increased hydraulic losses cause the feed pressure to decrease rapidly along the feed flow direction. Thus, the effect of the trans-membrane osmotic pressure is more prominent at higher feed flow rates and the net driving force is decreased. Further appreciation of

this trend of variation of net driving pressure can be obtained by observing its variation at any fixed point of the membrane with respect to flow rate. The net driving pressure at the mid-point of the membrane at different flow rates is shown in Fig. 3-7. . It is to be noted that the flow rate at which the net driving pressure is maximum will be different if a different inlet feed concentration is considered or different membrane properties are considered but the trend of variation with flow rate will be similar. Since the trans-membrane flux is directly dependent on the driving force, the variation of the trans-membrane flux is exactly similar to the driving force as clearly illustrated in Fig. 3-8.

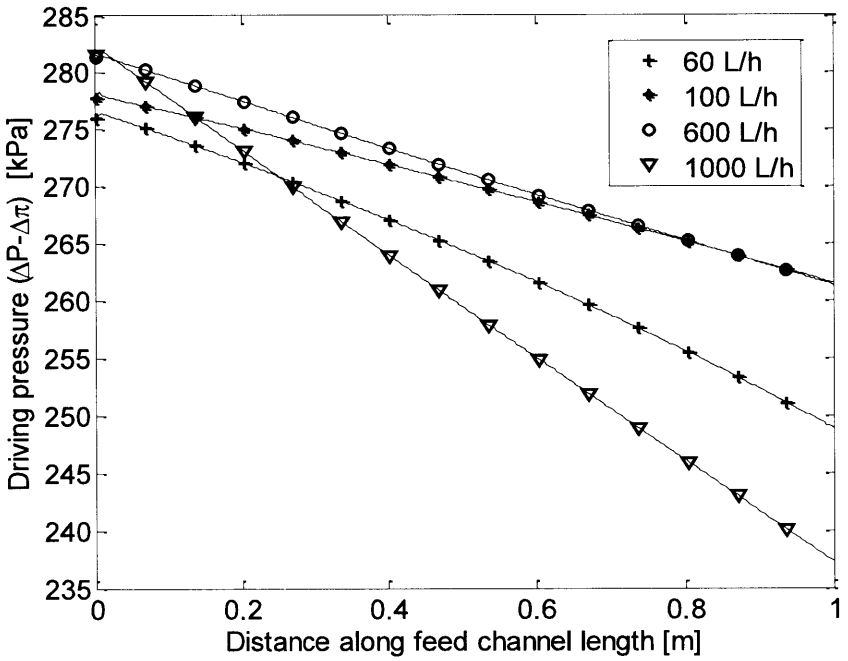

Fig. 3-6 Driving pressure along the membrane length, at 480 kPa inlet feed pressure and different flow rates.

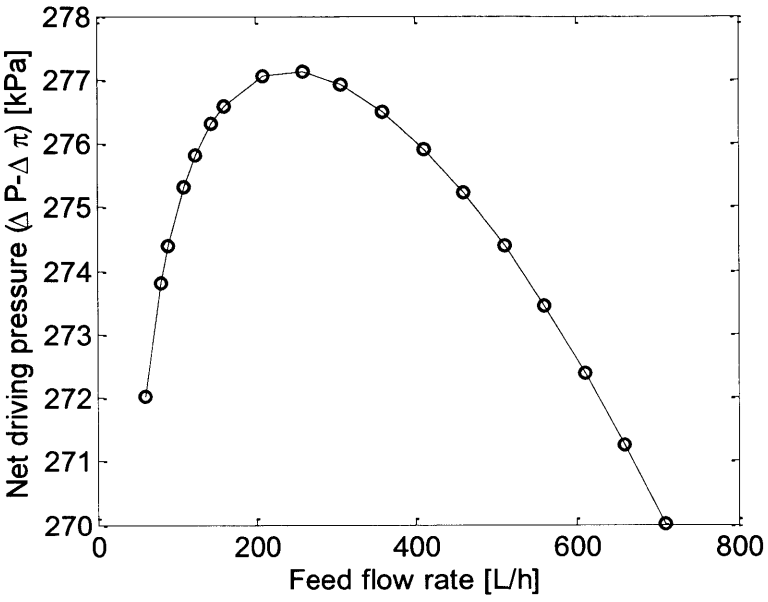

Fig. 3-7 Driving pressure at midpoint of the feed channel, at 480 kPa inlet feed pressure and different flow rates.

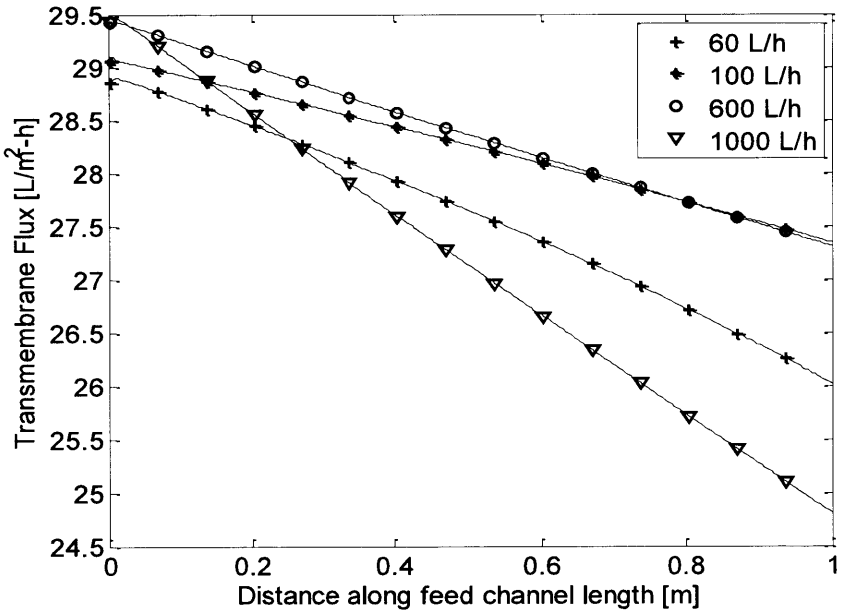

Fig. 3-8 Variation of transmembrane flux along feed flow direction at 480 kPa inlet feed pressure and different feed flow rates.

Figure 3-9 shows the variations of the overall rejection ratio of the membrane with the feed pressure. It is illustrated that the rejection ratio increases monotonically with the feed pressure. This is because the driving force is higher, causing solvent permeation to be higher, therefore 'leaving behind' the solute ions. In contrast, the rejection ratio increases with the flow rate but reaches an asymptotic value. This is because when increasing the flow rate, initially the driving force and hence the solvent permeation increases but as the flow rate is further increased, the driving force is decreased (due to the pressure drop and decrease in the osmotic pressure difference), causing lower solvent flux and hence decreased rejection. Figure 3-10 shows the variation of the net recovery ratio with flow rate at different feed pressures. As shown in this figure, at higher flow rates, the recovery ratio decreases. This is because the net driving pressure decreases, causing a decrease in the trans-membrane flux. Since the permeate flow is created by the flux coming in from the feed side, the decreased trans-membrane flux implies a reduced recovery ratio. Similarly, the recovery ratio increases with the feed pressure because the driving force for permeation increase causing a greater trans-membrane flux and hence greater recovery.

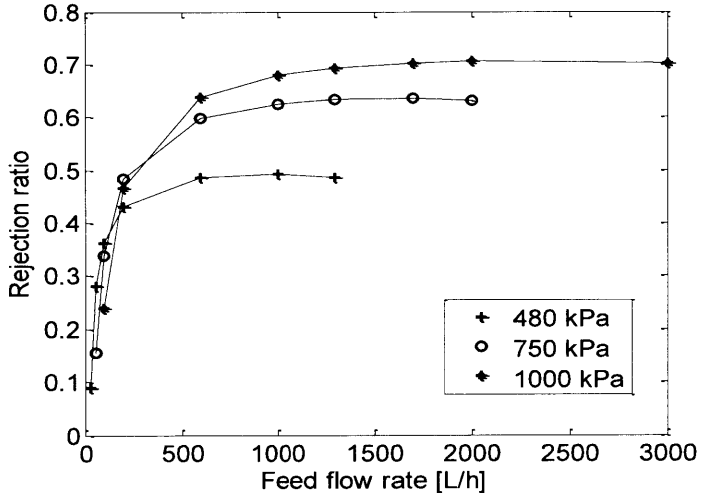

Fig. 3-9 Rejection ratio for NaCl at different feed flow rates and inlet feed pressures.

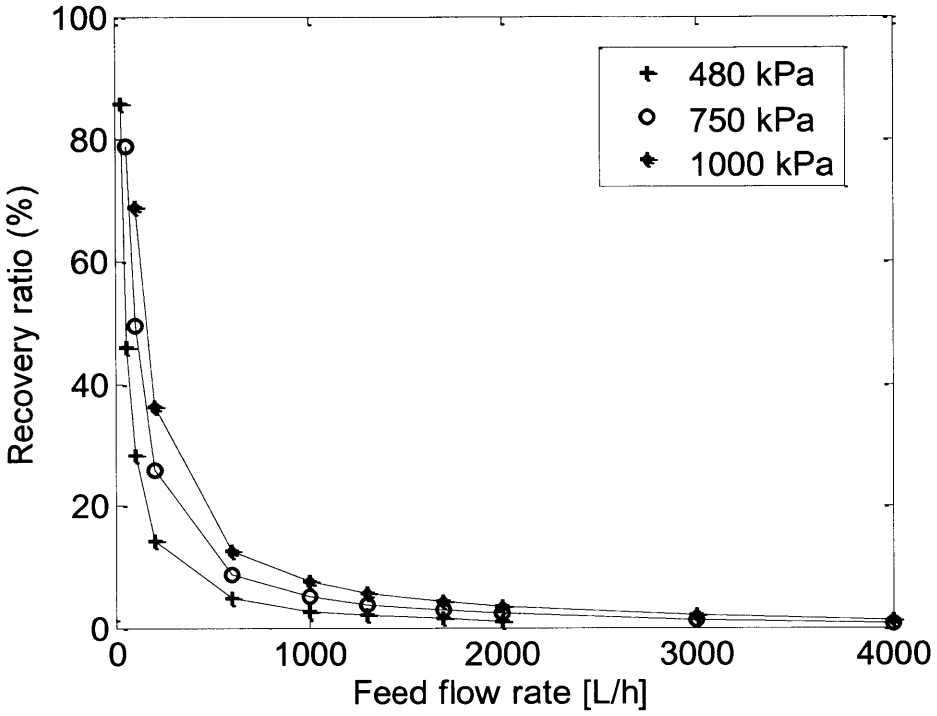

Fig. 3-10 Recovery ratio at different feed flow rates and inlet feed pressures.

3.2 Comparison between the flat-sheet and spiral-wound models

The operation of the spiral-wound membrane can be explained similarly to that of the flat-plate configuration. The trends of variation of quantities such as the Reynolds numbers, mass transfer coefficients, feed concentrations, rejection ratios and recovery ratio with respect to feed flow rate and feed pressure are similar to the flat-sheet case. The key difference is that in the spiral-wound module, these quantities also vary in the permeate-flow direction, perpendicular to the feed flow. To compare the performance of the spiral-wound membrane with the flat-sheet, Figs. 3-11, 3-12 and 3-13 show surface plots of the trans-membrane hydraulic pressure (TMP), rejection ratio, and trans-membrane flux in the two configurations under similar operating conditions (i.e. flow rate of 50 L/h, feed inlet pressure of 480 kPa, and 2000 ppm sodium-chloride feed). The spiral-wound membrane shows the maximum and minimum values of the TMP and flux at opposite corners of the membrane. The range of the three quantities plotted is similar in both the flat-sheet and spiral-wound membranes. Therefore, for identical leaf geometry and identical flow conditions, the flat-sheet and spiral-wound configurations give similar results. Since the computational model for the flat-sheet membrane is computationally less time consuming and less complex compared with the spiral-wound configuration, it would be advantageous to use the flat-sheet configuration model instead of the spiral-wound one without losing significant information.

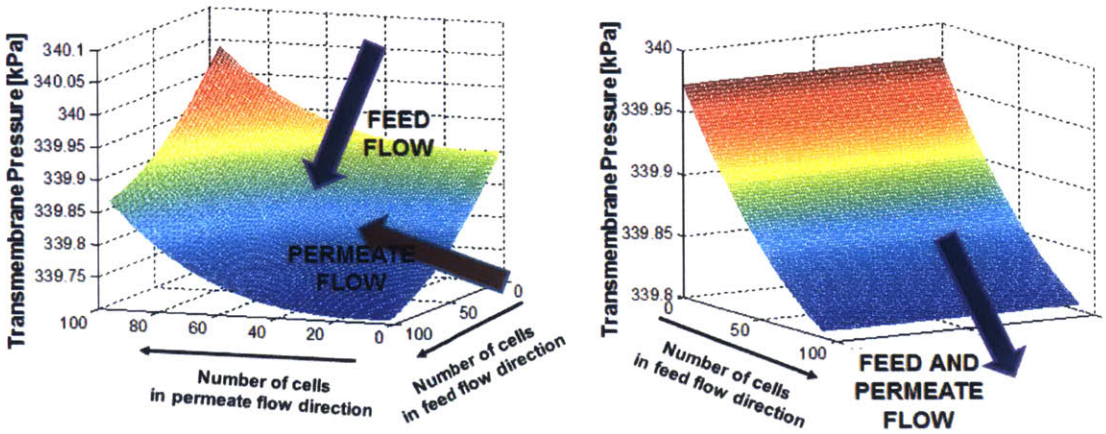

Fig. 3-11 Comparison of 2D characteristics values for spiral-wound membrane and flat-sheet membrane at 50 L/h feed flow rate and 480 kPa feed pressure with respect to trans-membrane pressure (TMP)

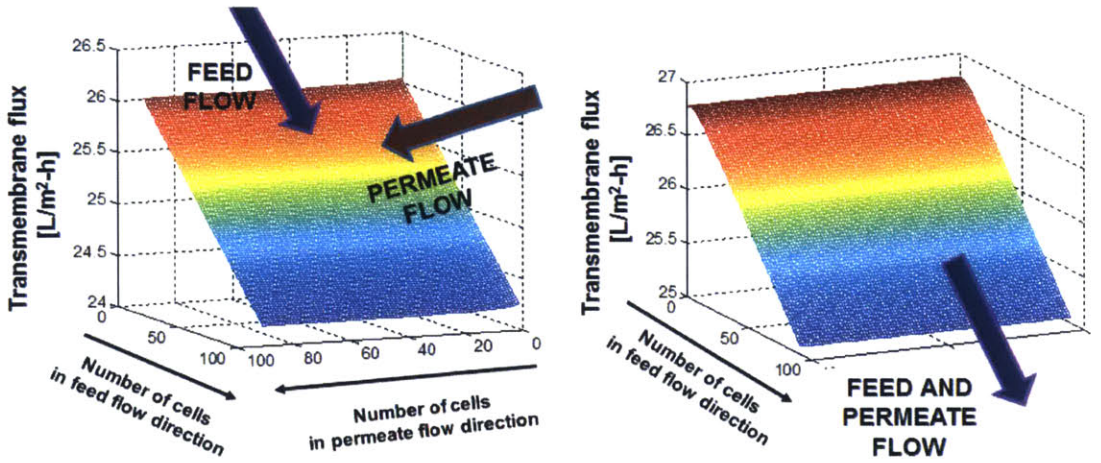

Fig. 3-12 Comparison of 2D characteristics values for spiral-wound membrane and flat-sheet membrane at 50 L/h feed flow rate and 480 kPa feed pressure with respect to transmembrane flux.

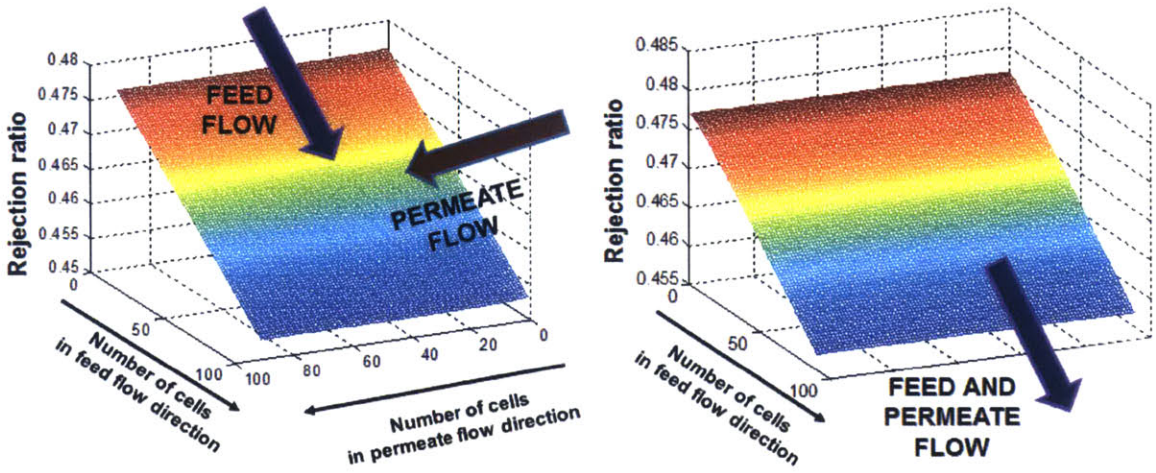

Fig. 3-13 Comparison of 2D characteristics values for spiral-wound membrane and flat-sheet membrane at 50 L/h feed flow rate and 480 kPa feed pressure with respect to rejection ratio.

To investigate this further, it is necessary to check if under different flow conditions, the variation of quantities in the permeate flow direction is significant. Four flow rates spread over a wide range, 1805 L/h, 361L/h, 110 L/h and 50L/h were investigated at different values of feed inlet pressures (480 kPa, 750 kPa and 1000kPa) and 2000 ppm sodium-chloride solution was considered. It was observed that the variation of the feed flow rate, net driving pressure, trans-membrane flux, rejection ratio, and feed concentration in the direction of permeate flow (percentage variation from beginning of permeate flow to the permeate exit) is less than 10% in all cases and less than 5% in most cases. The only quantity that shows marked variation along

the permeate flow direction is the permeate Reynolds number which has a maximum value of about 20 at the feed entrance, near the permeate exit. It is close to zero along the edge of the leaf where the permeate flow begins.

Therefore, it can be concluded that for similar geometric specifications, the computationally less intensive flat-sheet model introduced in this work can be used to predict the performance of the spiral-wound membrane. This observation is especially helpful for the investigation of large scale-systems where series of spiral-wound membrane elements are used. Since in a membrane element the spiral-wound leaves are in parallel, the rejection ratio and recovery ratio for the entire element is the same as that of the individual leaf. In order to model a series of elements, the modeling can be simply made so that the exit feed flow rate and pressure will be the inlet values for the next element.

3.3 Modeling seawater nanofiltration

The model of nanofiltration introduced in this work is now applied to seawater and it is validated with respect to a large scale desalination system, the Umm Lujj NF-SWRO plant owned by the Saline Water Conversion Corporation, Research and Development Center (SWCC-RDC) [40], [41]. Gulf seawater concentration [26], as shown in Table 3.1, is used as the initial feed solution.

The setup of the Umm Lujj NF unit described in the references is modeled, and it is attempted to match the overall recovery ratio and rejection ratio for each individual ion when the flow conditions as specified in [40] are applied. The nanofiltration unit of the desalination plant described in references [40] and [41], consists of several pressure vessels in parallel. Each vessel

consists of six spiral-wound elements of the DK8040F membrane manufactured by GE-Osmonics, in series.

Table 3.1 Validation of solute rejection ratios from model for sea-water nanofiltration in a large scale desalination plant

Ion	Concentration in seawater (ppm)	Rejection ratio [33]	Rejection ratio from present model	% Deviation
Ca^{2+}	491	91	90.65	0.384
Mg^{2+}	1556	98	99.39	-1.41
SO_4^{2-}	3309	99.9	93.50	6.40
Cl^-	23838	24	27.73	-15.54
HCO_3^-	155.5	56	49.44	11.71

Since the pressure vessels operate in parallel, the rejection ratio and recovery ratio of the entire NF unit is represented by the values obtained for a single vessel. In order to model a pressure vessel, six elements are modeled such that the exit feed pressure and flow rate from each element is the inlet for the next element. The inlet feed pressure and inlet feed flow rates are taken as 30 bar and 13.3 m^3/h respectively, which are the values given for each vessel in [40]. The recovery ratio in each vessel in [40] was found to be 65%.

Since the NF unit described in the Umm Lujj plant [40] [41] uses DK4080F membrane which fall under the broad category of Desal-DK membranes manufactured by GE-Osmonics, it is necessary to obtain the membrane characteristics which give a good fit with the DSPM-DE model. In this simulation, the results from the characterization of Desal-DK membranes given in references [5], [7] are used. They found the pore radius to be 0.45 nm and the active layer thickness to porosity ratio ($\Delta x / A_k$) of 3μm (when characterized by glucose). In addition, the pore dielectric constant is found to be 38. However, in order to obtain good correspondence with the data in [40], values of pore dielectric constant and membrane charge density are set to $\varepsilon_{pore} = 56.5$ and $C_X = -80$ mol/m^3. The deviation of the pore dielectric constant from the value in literature may be due to the fact that in the references, the fitting is done with respect to the rejection data of a single solute such as sodium-chloride, whereas in seawater there is a mixture of ions, each of which has its own unique behavior with the membrane. The interaction of different solutes with the same membrane can indeed be very different. For example, in [20] (Table 4), it is found that the dielectric constant of the membranes NF99HF and NF270 is around 40 from characterization with respect to sodium-chloride, potassium-chloride, and sodium-sulphate, while magnesium-sulphate gives a value around 75 for NF99HF and 65 for NF270, thereby indicating that this salt has a unique chemistry with the membrane [20]. In addition, in

[21] (Table 2), it is seen that characterization of volumetric charge density for the both the membranes NF300 and NF250 with respect to sodium-chloride are negative, while fitting with respect to magnesium-chloride gives a positive membrane charge density. Since seawater contains not only sodium, chloride, sulphate, and magnesium ions, but also several other ions, it is expected that the final values of the pore dielectric constant and membrane charge to be an 'average' value that represents the interaction of all these ions with the membrane.

Furthermore, the membrane charge density changes with solute concentration and therefore will vary from element to element in the series. However, in order to find a relation for the variation of membrane charge density as a function of feed concentration as done in [21] for seawater, a few experiments need to be performed, which is beyond the scope of our research thus far. As mentioned previously, a simple correlation between solute concentration and membrane charge density can be obtained from experimental analysis. However, for seawater the situation is made more complex by the fact that it contains a variety of solute ions and the type of correlation varies from solute to solute. For example, in [42], the charge-concentration correlation for calcium-chloride is found to be almost parabolic while that for sodium-chloride is linear. Therefore, to simplify the situation, the same value of membrane charge density for all the six elements is taken for the simulation.

As mentioned earlier, even though a charge density for all the elements in series is considered, which is not completely rigorous, the present model is able to predict the relative values of rejection of each ion with respect to the others correctly; and, for the flow parameters used in the Umm Lujj plant, the model is able to correctly predict the recovery ratio. Further

experimentation to correlate seawater concentration with membrane charge will fine-tune the values of rejection ratio of each ion and improve the agreement with experimental values. As observed in the Table 2, there is a good agreement of values and trends with the reference. A recovery ratio of 65.41% for each vessel is obtained, which has an error of only 0.63% with respect to the reference. Thus our model can be used with confidence in the modeling of seawater nanofiltration.

THIS PAGE IS INTENTIONALLY LEFT BLANK

Chapter 4

Conclusions

4.1 Major conclusions

In this work, a comprehensive 2D model for large-scale NF membranes is developed by extending the DSPM-DE model over a membrane leaf. The effect of flow parameters such as feed pressure and flow rate on the solute rejection and recovery ratio of the membrane has been investigated. The variation of other quantities such as feed concentration, permeate concentration and trans-membrane flux along the feed flow direction have also been presented. These studies have shown that the rejection and recovery ratios of the NF membrane ultimately depend on the net driving pressure across the membrane. An analysis of how the driving pressure is affected by the feed flow conditions is made. It is shown that the net driving pressure increases with feed pressure and beyond a certain point and decreases with feed flow rate.

Two configurations for nanofiltration membranes, namely flat-sheet and spiral-wound have been modeled. These configurations are distinguished by the feed and permeate flow arrangements. In flat-sheet modules, the feed and permeate flows in their respective channels are parallel to each other, while in the spiral-wound case, the feed and permeate flow are perpendicular to one-another. Our work shows that for similar geometric properties, under similar operating conditions, the spiral-wound and flat-sheet configurations perform similarly. This observation is significant because although the spiral-wound configuration is commercially more common, it is computationally more expensive and complicated. The ability of the flat-

sheet model to predict the performance of the spiral-wound configuration greatly reduces the computational expense.

Our work also shows that for reasonable values of fit of membrane characterization parameters with respect to the DSPM-DE model, the performance of nanofiltration membranes for seawater desalination can be accurately predicted. This is established by validating the model introduced with results from a large-scale desalination plant. The establishment of the model as a reliable means to simulate the performance of nanofiltration in large-scale systems opens the doors for the investigation of NF in several processes, over a wide range of operating conditions, whether it is in a desalination system or in any of several other applications, without excessive dependence on experimental data.

4.2 Further work motivated by this thesis

Further work is needed, however, in finding a means to characterize how membrane charge densities vary with concentration of seawater ions or for any other feed solution. This will give a more accurate prediction of seawater nanofiltration when several membrane elements are in series. Membrane charge characterization as a function of concentration will require experiments which determine the rejection of ions versus applied pressure for different initial feed concentrations [7] [21]. One can then fit the charge density for different ratios of seawater ions to water in solution, which can then be tied together by a relation obtained by fitting to get membrane charges over a large range of concentrations.

THIS PAGE IS INTENTIONALLY LEFT BLANK

Appendix A

1. Flat-sheet model for nanofiltration:

```
clear all                          %Clear workspace from previous simulations
clc
%Experimental Setup:
Length = 1;                        %Length of Membrane[m]
Width = 1;                         %Width of Membrane [m]
Height_B = 7e-4;                   %Height of Feed Channel [m]
Height_P = 3e-4;                   %Height of Permeate Channel [m]
RP = 4.30e-10;                     %Membrane Pore Radius [m]
DELTA = 1e-6;                      %Thickness of membrane active layer [m]
Cells = 300;
Cell_Length = Length/Cells;        %Length of each Cell [m]
%Input values:
NC = 2;                            %Number of Ions
ND = 105;                          %Number of Discretization Points inside
membrane
Flow_B = [1.67e-5];                %Inlet flow rate of Feed (first cell) [m^3/s]
Flow_P = [0];                      %Inlet flow rate of Permeate (first cell)
[m^3/s]
CIB = [34, 34];                    %Inlet Feed Concentration (first cell)
[mol/m^3]
%CIB = [18, 36];
Pressure_Feed = [0.48e6];          %Inlet Feed Pressure(first cell) [Pa]
Pressure_Permeate = 1e5;           %Permeate channel pressure (uniform)[Pa]
CP_Cell = zeros(1,NC);             %Initialization of average permeate
concentration in cell
D = [1.33; 2.03]*1e-9;             %Ion Diffusivity in Bulk solution [m^2/s]
%D = [0.92; 2.03]*1e-9;
K = .5;                            %Mixing Efficiency of Net
L_mix = .006;                      %Characteristic length of mixing net [m]
RHO = 1000;                        %Density of water [kg/m^3]
R = 8.314;                         %Universal gas constant [J/(mol-K)]
T = 298;                           %Temperature [K]
MU = .798e-3;                      %Dynamic Viscosity of solvent (water) [Pa-s]
Eff = .5;                          %Pump efficiency


%Calculated quantities
```

```
Contact_Surf = Width*Cell_Length;              %Contact surface area of
feed/permeate channels with membrane in each cell [m^2]
Cross_AreaB = Height_B*Width;                  %Cross sectional area of feed
channel[m^2]
Cross_AreaP = Height_P*Width;                  %Cross sectional area of permeate
channel [m^2]
Velocity_Feed = [Flow_B/Cross_AreaB];          %Velocity of feed [m/s]
Velocity_Permeate = Flow_P/Cross_AreaP;        %Velocity of permeate[m/s]
Pe = [2*Height_B*Velocity_Feed./D]';           %Peclet Number
L_C = 4*Cross_AreaB/(2*Width+2*Height_B);      %Characteristic length of Cell (for
Reynolds Number Calculation)- hydraulic diameter.
Delta_P= [Pressure_Feed-Pressure_Permeate];    %Transmembrane Pressure [Pa]
JV = RP^2*(Delta_P)/8/MU/DELTA;               %Initial transmembrane flux (first
cell) [m^2/s]

for i = 1:Cells
i
    if ~(i==1)
        %f(i) = 96/RE_list(i-1);
        f(i) = 6.23/(RE_list(i-1))^0.3;
  Pressure_Feed(i) = Pressure_Feed(i-1) - f(i)*Velocity_Feed(i-
1)^2*RHO/L_C/2*Cell_Length;
        Osmotic_Feed(i) =  R*T*sum(CI0_list(i-1,:));
        Osmotic_Permeate(i) = R*T*sum(CIP(i-1,:));
        Delta_Osmotic_Pressure(i) = Osmotic_Feed(i)-Osmotic_Permeate(i);
        Delta_P(i) = Pressure_Feed(i)-Pressure_Permeate;
    end

    if ((i==1) || (i==2))
        JV(i) = RP^2*(Delta_P(i))/8/MU/DELTA;
    else
        JV(i) = RP^2*(Delta_P(i)-Delta_Osmotic_Pressure(i))/8/MU/DELTA;
    end

    if ~(i==1)
        Flow_B(i) = Flow_B(i-1) - .5*(JV(i)+JV(i-1))*Contact_Surf;
        Flow_P(i) = Flow_P(i-1) + .5*(JV(i)+JV(i-1))*Contact_Surf;
        Velocity_Feed(i) = Flow_B(i)/Cross_AreaB;
        Velocity_Permeate(i) = Flow_P(i)/Cross_AreaP;
        Pe(i,:) = 2*Height_B*Velocity_Feed(i)./D;
```

```
        CIB(i,:) = (Flow_B(i-1).*CIB(i-1,:) - .5*CIP(i-1,:)*(JV(i)+JV(i-
1))*Contact_Surf)/Flow_B(i);
        CP_Cell(i,:) = (Flow_P(i-1).*CP_Cell(i-1,:) + .5*CIP(i-1,:)*(JV(i)+JV(i-
1))*Contact_Surf)/Flow_P(i);
    end


%% Overall Paramaters

EMEMB = 40.4;                       %Dielectric Constant of Pore
EWATER = 80.4;                      %Dielectric Constant of Water
EPSX = 1;                           %Mesh Expansion Factor
F = 96500.0;                        %Faraday Constant [C/Eq]
ITMAX = 5000;                       %Max number of iterations
NCX = 100;                          %Max Number of Ions
NDX = 5000;                         %Max Number of Nodes
NV = (ND+1)*(NC+1);                 %Number of Variables
NVX = (NDX+1)*(NCX+1);              %Max Number of variables
R = 8.314;                          %Molar Gas Constant [J/(mol*K)]
SMALL = 1e-15;                      %Small Value Parameter
TOL = 1.00e-4;                      %Maximum normalized Residual
URF = .2;                           %Under Relaxation Factor
KF = F/(R*T);                       %Ratio for better calculations [C/J]
NU = 8.97e-7;                       %Kinematic Viscosity of solvent (water)
RE = Velocity_Feed(i)*L_C/NU;       %Reynolds Number
RE_P(i) = Velocity_Permeate(i)*4*Cross_AreaP/(2*Width+2*Height_P)/NU; %Reynolds
number of permeate


%% Ion data
Z = [1; -1];                    %Ionic Charge
%Z = [2; -1];
RS = [1.84; 1.21]*1e-10;        %Ionic radii [m]
%RS = [3.09; 1.21]*1e-10;
CX = -10.5;                       %Membrane Charge [mol/m^3]
CI0 = CIB(i,:);                 %Initialization of membrane concentration

%% Computation of Hindrance Factors and Steric Partition Coefficients
for IC=1:NC
```

```
    RL(IC) = RS(IC)/RP;                %Ionic radius to pore radius ratio
    PHIL(IC) = (1-RL(IC))^2;           %Partition Factor due to Steric Exclusion

    if (RL(IC)>=1.0)
        PHIL(IC) = SMALL;
        KDF(IC) = 1e-8;               %Hindrance Factor for Diffusion
        KCV(IC) = 1e-8;               %Hindrance Factor for Convection
    end

    if (RL(IC) <= .95)
        KDF(IC) = (1+ 9/8*RL(IC)*log(RL(IC)) -1.56034*RL(IC)+.528155*RL(IC)^2 ...
                  +1.91521*RL(IC)^3-2.81903*RL(IC)^4 + 0.270788*RL(IC)^5 + ...
                  1.10115*RL(IC)^6 - 0.435933*RL(IC)^7)/(1-RL(IC))^2;
        KCV(IC) = (1+3.867*RL(IC)-1.907*RL(IC)^2-.834*RL(IC)^3)/(1+1.867*RL(IC)-
.741*RL(IC)^2);
    end

    if (.95 < RL(IC) && RL(IC) < 1.0)
        KDF(IC) = .984*((1-RL(IC))/RL(IC))^(2.5);
        KCV(IC) = (1+3.867*RL(IC)-1.907*RL(IC)^2-.834*RL(IC)^3)/(1+1.867*RL(IC)-
.741*RL(IC)^2);
    end

    DM(IC) = KDF(IC)*D(IC);            %Ion Diffusivity in the Membrane Active
layer[m^2/s]
    U(IC) = DM(IC)*KF;                 %Ion Mobility Inside Membrane [sqrt(C)/kg]


end
%% Mesh Generation
if (EPSX <= 1.0)
    EPSX = 1.0000001;
end
XM(ND) = DELTA;
XM(ND-1) = DELTA;
DX = DELTA/2/((1-EPSX^((ND-2)/2))/(1-EPSX));
for I=1:(ND-3)
    XM(ND-I-1)= XM(ND-I)-DX;
    DX = EPSX*DX;
end
```

```
XM(1) = 0;
for I = 1:(ND/2)
    XM(I)=DELTA-XM(ND-I);
    DX = EPSX*DX;
end

%% Mass Transfer Coefficient Correction, Steric and Dielectric Exclusion
for IC=1:NC

    DH(IC) =  6.95e-5*Z(IC)^2/RS(IC)*(1/EMEMB-1/EWATER);          %Born solvation
energy barrier [J]
    SC(IC) = NU/D(IC);                                            %Schmidt number
    if (i==1)
        Entry_Length(IC) = .05*L_C*SC(IC)*RE;                     %Calculate Entry
KC(IC) =.753*(K/(2-K))^.5*D(IC)/Height_B*SC(IC)^(-
1/6)*(Pe(i,IC)*Height_B/L_mix)^(.5);
    if (KC(IC) == 0)
        KC(IC) = 10;
    end
    KPHI(IC) = JV(i)/KC(IC);                                      %Temporary
Variable for Calculating KCDOT
    KCDOT(IC) = KC(IC)*(KPHI(IC)+ (1+.26*KPHI(IC)^1.4)^(-1.7));  %Corrected Mass
Transfer Coefficient
    PHILE(IC) = exp(-DH(IC)/(R*T));



end

for I=1:ND              %Initialize Concentrations to feed concentration in NCxND
Matrix
    CI(:,I)= CIB(i,:);
end

PHI = zeros(1,ND);      %Initialize PHI to be all zeros
DPHIDX = 0;             %Initialize potential gradient at membrane surface one feed
side as zero.
A = zeros(NV);          %Initialize Matrix A
B = zeros(NV,1);        %Initialize Matrix B

%% Coefficient Assembly
```

```
 for JITER = 1:ITMAX
%N-P Discretization Equations
 IEQ = 0;
    for IC =1:NC
        for I=1:(ND-2)
            DX = XM(I+1)-XM(I);
            IEQ = IEQ+1;
            A(IEQ,(IC-1)*ND+I) = DM(IC)/DX + .5*JV(i)*KCV(IC) -
.5*Z(IC)*U(IC)*(PHI(I+1)-PHI(I))/DX;
            A(IEQ,(IC-1)*ND+I+1) = -DM(IC)/DX + .5*JV(i)*KCV(IC) -
.5*Z(IC)*U(IC)*(PHI(I+1)-PHI(I))/DX;
            A(IEQ, NC*ND+I) = .5*Z(IC)*U(IC)*(CI(ICI+1)+CI(IC,I))/DX;
            A(IEQ, NC*ND+I+1) = -.5*Z(IC)*U(IC)*(CI(IC,I+1)+CI(IC,I))/DX;
            A(IEQ, IC*ND) = -JV(i);
            B(IEQ, 1) = -Z(IC)*U(IC)*.5*(CI(IC,I+1)+CI(IC,I))*(PHI(I+1)-PHI(I))/DX;
        end
    end
 %Charge Balance
     for I = 1:ND
        IEQ = IEQ+1;
        for IC = 1:NC
            A(IEQ, (IC-1)*ND+I) = Z(IC);      %for each ion, the charge is also
included in the overall A Matrix
        end
        if (I ~= ND)
            B(IEQ,1) = -CX;                   %the B Matrix holds the overall
membrane charge
        end
    end
 %Feed-Membrane Equilibrium
     RIFB = 0;
    RIFM = 0;


    for IC = 1:NC
        RIFB = RIFB + 0.5*Z(IC)^2*CI0(IC)/1000;          %Ionic Strength Parameters
        RIFM = RIFM + 0.5*Z(IC)^2*CI(IC,1)/1000;
    end
    ABULK = 1.825E6*(1/EWATER^3/T^3)^(.5);
    AMEMB = 1.825E6*(1/EMEMB^3/T^3)^(.5);


%Activity Coefficients
```

```
    for IC = 1:NC
        IEQ = IEQ + 1;
        GAMAB = exp(-ABULK*Z(IC)^2*(RIFB^.5/(1+RIFB^.5)-0.3*RIFB));      %Activity
coefficient equation 12
        GAMABM = exp(-AMEMB*Z(IC)^2*(RIFM^.5/(1+RIFM^.5)-.3*RIFM));
        if (Z(IC) == 0)
            GAMAB = exp(.1*RIFB);
            GAMABM = exp(.1*RIFM);
        end
        GB(IC) = GAMAB/GAMABM;
        KE1 = PHIL(IC)*PHILE(IC)*GB(IC)*exp(-Z(IC)*KF*PHI(1));
        A(IEQ,(IC-1)*ND+1) = 1.0;
        A(IEQ, NC*ND+1) = CI0(IC)*Z(IC)*KF*KE1;
        B(IEQ,1) = CI0(IC)*KE1*(1+Z(IC)*KF*PHI(1));
    end
% Membrane- Permeate Equilibrium
     RIFB = 0;
    RIFM = 0;
    for IC = 1:NC
        RIFB = RIFB + .5*Z(IC)^2*CI(IC,ND)/1000;         %Ionic Strength
        RIFM = RIFM + .5*Z(IC)^2*CI(IC, ND-1)/1000;
    end


    for IC = 1:NC
        IEQ = IEQ+1;
        GAMAP = exp(-ABULK*Z(IC)^2*(RIFB^.5/(1+RIFB^.5)-.3*RIFB));
        if (Z(IC) ==0)
            GAMAP = exp(.1*RIFB);
        end
        GAMAPM = exp(-AMEMB*Z(IC)^2*(RIFM^.5/(1+RIFM^.5)-.3*RIFM));
        if (Z(IC) ==0)
            GAMAPM = exp(.1*RIFM);
        end


        GP(IC) = GAMAP/GAMAPM;                           %Ratio of strengths
        KE2 = PHIL(IC)*PHILE(IC)*GP(IC)*exp(Z(IC)*KF*(PHI(ND)-PHI(ND-1)));
%Equation 33
        A(IEQ, ND*IC-1) = 1/CI(IC,ND);
        A(IEQ, ND*IC) = -KE2/CI(IC,ND);
        A(IEQ, ND*(NC+1)-1) = Z(IC)*KF*KE2;
```

```
        A(IEQ,ND*(NC+1)) = -Z(IC)*KF*KE2;
        B(IEQ,1) = KE2*(-Z(IC)*KF*(PHI(ND)-PHI(ND-1)));

    end

%Feed Membrane Mass Transfer Resistance

    for IC = 1:NC
        IEQ = IEQ + 1;
        A(IEQ, ND*(NC+1)+IC) = KCDOT(IC) - JV(i);
        A(IEQ,IC*ND) = JV(i);
        A(IEQ, (ND+1)*(NC+1)) = Z(IC)*KF*D(IC)*CI0(IC);
        B(IEQ,1) = KCDOT(IC)*CIB(i,IC);
    end

%Feed Membrane Interface Charge Balance

    IEQ = IEQ + 1;

    for IC = 1:NC
        A(IEQ, ND*(NC+1)+IC) = Z(IC);
    end

    B = A\B;        %Matrix Solver
    x = B;

%Under Relaxation
    for I = 1:ND
        for IC = 1:NC
            DCI = (B((IC-1)*ND+I,1) - CI(IC,I))/(CI(IC,I));
            if (abs(DCI) > 1)
                DCI = abs(DCI)/DCI;
            end
            CI(IC,I) = CI(IC,I)*(1+URF*DCI);
        end
        PHI(I) = PHI(I)+ URF*(B(NC*ND+I,1)-PHI(I));
        if (abs(PHI(I))>5)
        PHI(I) = 0;
        end
    end
```

```
    for IC = 1:NC
        DCI = (B(ND*(NC+1)+IC,1)-CI0(IC))/CI0(IC);
        if(abs(DCI)>1)
            DCI = abs(DCI)/DCI;
        end
        CI0(IC)= CI0(IC)*(1+URF*DCI);
   end
    DPHIDX = DPHIDX+URF*(B((ND+1)*(NC+1),1) - DPHIDX);
    if (abs(DPHIDX)>500)
        DPHIDX= DPHIDX/abs(DPHIDX);
    end


%Re-Initializing Matrices
    A = zeros(NV);
    B = zeros(NV,1);


%%Residual Computations


    for IC = 1:NC
        RESCI(IC) = 0;
    end


    RESEQ = 0;
    RESBAL = 0;
    for I = 1:(ND-2)
        for IC = 1:NC
            DX = XM(I+1)-XM(I);
            RESCI(IC) = RESCI(IC)+ abs(-DM(IC)*(CI(IC,I+1)-CI(IC,I))/DX ...
                -.5*Z(IC)*U(IC)*(CI(IC,I+1)+CI(IC,I))*(PHI(I+1)-PHI(I))/DX ...
                +.5*JV(i)*KCV(IC)*(CI(IC,I+1)+CI(IC,I)) - JV(i)*CI(IC,ND)); %
Numerator Equation 38
        end
        SUMC = 0;
        for IC = 1:NC
            SUMC = SUMC+ Z(IC)*CI(IC,I);
        end
        RESBAL = RESBAL+ abs(SUMC + CX);
    end
```

```
    for IC=1:NC
        if (PHIL(IC)<=SMALL)
            RESCI(IC) = 0;
        end
    end

    SUMC = 0;
    SUMCP = 0;
    SUMCTB = 0;
    for IC =1:NC
        SUMC = SUMC+Z(IC)*CI(IC,ND-1);
        SUMCP = SUMCP+Z(IC)*CI(IC,ND);
        SUMCTB = SUMCTB+abs(Z(IC)*CIB(i,IC));
    end
    RESBAL = RESBAL + abs(SUMC+CX)+abs(SUMCP);
    RESBAL = RESBAL/(SUMCTB +abs(CX));
    RJT = 0;
    for IC = 1:NC
        RJT =  RJT + abs(JV(i)*CI(IC,ND));
    end
    for IC = 1:NC
        RESCI(IC) = RESCI(IC)/RJT;
    end

    %% Compute KC Residual
    if (KC(1) < 10)
        RESKC = 0;
        for IC = 1:NC
            RESKC = RESKC + abs(JV(i)*CI(IC,ND)+KCDOT(IC)*(CI0(IC)-
CIB(i,IC))+Z(IC)*KF*D(IC)*CI0(IC)*DPHIDX-JV(i)*CI0(IC))/RJT;
        end
    else
        RESKC = 0;
    end


    for IC = 1:NC
        if (PHIL(IC) > 1e-10)
            KE1 = PHIL(IC)*PHILE(IC)*GB(IC)*exp(-Z(IC)*KF*PHI(1));
            KE2 = PHIL(IC)*PHILE(IC)*GP(IC)*exp(-Z(IC)*KF*(PHI(ND-1)-PHI(ND)));
            RESEQ = RESEQ + abs((CI(IC,1)/CI0(IC)/KE1)-1);
```

```
            if (CI(IC,ND) > 1e-11)
                RESEQ = RESEQ + abs((CI(IC,ND-1)/CI(IC,ND)/KE2)-1);
            end
        end
    end

    RM = 0;
    for IC = 1:NC
        if (RESCI(IC)>RM)
            RM = RESCI(IC);
        end
    end

    if (max([RM,RESBAL,RESKC, RESEQ]) < TOL)
        break
    end
end

% for IC = 1:NC
%     figure(IC); clf; plot(XM(1:ND-1),CI(IC,1:ND-1))%plot model and points
%     % format the plot
%     axis([0 DELTA min(CI(IC,1:ND-1))*.9999999
max(CI(IC,:))*1.0000001]);title('Concentration Values Through the Membrane');
xlabel('Membrane Position [m]'); ylabel('Concentration [mol/m^3]')
% end
%Computing Rejection Rates

for IC = 1:NC
    RREAL(IC) = (CI0(IC)-CI(IC,ND))/CI0(IC);
    ROBS(IC) = (CIB(i,IC)-CI(IC,ND))/CIB(i,IC);
    if ~(i==1)
    RCP(IC) = (CIB(i,IC)-CP_Cell(i,IC))/(CIB(i,IC));
    end
end
if ~(i==1)
RCP_List(i,:) = RCP(:);
end

CI0_list(i,:) = CI0;
```

```
ROBSERVED(i,:) = ROBS(:);
CIP(i,:) = CI(:,ND)';
List_iters(i)=JITER;
RESBAL_list(i) = RESBAL;
RESKC_list(i) = RESKC;
RESEQ_list(i) = RESEQ;
RESCI_list(i,:) = RESCI(:);
KC_list(i,:) = KC(:);
%SH_list(i,:) = SH(:);
SC_list(i,:) = SC(:);
RE_list(i) = RE;

end
RMEAN = mean(ROBSERVED);                                    %Mean rejection ratio
RR = Flow_P(Cells)/Flow_B(1);                               %Recovery ratio
Power = 1/Eff*Flow_B(1)*(Pressure_Feed(1)-Pressure_Permeate);
```

2. Spiral-wound model for nanofiltration:

```
clear all                              %Clear workspace from previous
simulations
clc


%Experimental Setup:
Cells = 100;                           %Number of Cells in each direction
Length = 1;                            %Length of Membrane[m]
Width = 1;                             %Width of Membrane [m]
Height_B = 7e-4;                       %Height of Feed Channel [m]
Height_P = 3e-4;                       %Height of Permeate Channel [m]
RP = 4.30e-10;                         %Membrane Pore Radius [m]
DELTA = 1e-6;                          %Thickness of membrane active layer
[m]
Cell_Length = Length/Cells;            %Length of each Cell [m]
Cell_Width = Width/Cells;              %Width of each Cell [m]
NC = 2;                                %Number of Ions
ND = 105;                              %Number of Discretization Points
inside membrane
Feed_CIB = [34,34];                    %Initial Feed Concentrations
CIB = zeros(Cells,NC,Cells);           %Initialize Concentration Matrix
R = 8.314;                             %Molar Gas Constant [J/(mol*K)]
RHO = 1000;                            %Density of water [kg/m^3]
T = 298;                               %Temperature [K]
```

```
MU = .798e-3;                          %Dynamic Viscosity of solvent (water)
[Pa-s]
Cross_AreaB = Height_B*Cell_Width;     %Cross sectional area of cell in feed
channel[m^2]
Cross_AreaP = Height_P*Cell_Length;    %Cross sectional area of cell in
permeate channel [m^2]
Eff = .5;                              %Pump Efficiency

for IC = 1:NC
    CIB(1,IC,:) = Feed_CIB(IC);
end

Flow_P = zeros(Cells,Cells);
Flow_B = zeros(Cells,Cells);
Flow_P(:,1) = 0;
Flow_B(1,:) = 0.4e-4/Cells;
Velocity_Feed = Flow_B/Cross_AreaB;            %Velocity in cell in feed
[m/s]
Velocity_Permeate = Flow_P/Cross_AreaP;        %Velocity in cell in
permeate[m/s]
Pressure_Feed(1,:) = 1e6*ones(1,Cells);        %Inlet Feed Pressure(first
row) [Pa]
Pressure_Permeate=140100*ones(Cells,2);        %Permeate channel pressure
(first two columns)[Pa]
CP_Cell = zeros(Cells,NC,Cells);               %Initialization of average
permeate concentration in cell
Delta_Osmotic_Pressure = [R*T*sum(CIB(1,1))]; %Permeate concentration in
first cell initialized place holder
Delta_P= Pressure_Feed(1,1)-Pressure_Permeate(1,1);   %Transmembrane
Pressure [Pa]
JV = RP^2*(Delta_P)/8/MU/DELTA;                %Initial transmembrane flux
(first cell) [m^2/s]

for j = 1:Cells

j
```

```
%Input values:
KFF = 18.36e8;                          %Friction factor in feed channel
D = [1.33; 2.03]*1e-9;                  %Ion Diffusivity in Bulk solution
[m^2/s]
K = .5;                                 %Mixing Efficiency of Net
L_mix = .006;                           %Characteristic length of mixing net
[m]
R = 8.314;                              %Universal gas constant [J/(mol-K)]

%Calculated quantities
Contact_Surf = Cell_Width*Cell_Length;          %Contact surface area of
feed/permeate channels with membrane in each cell [m^2]
L_C = 4*Width*Height_B/(2*Width+2*Height_B);    %Hydraulic diameter of
feed channel
L_P = 4*Length*Height_P/(2*Length+2*Height_P);  %Hydraulic diameter of
permeate channel


for i = 1:Cells


    if ~(i==1)
        Osmotic_Feed(j,i) =  R*T*sum(CI0_list(j,:,i-1));
        Osmotic_Permeate(j,i) = R*T*sum(CP_Cell(j,:,i-1));
    end

    if (i==1)
        Osmotic_Feed(j,i) = 0;
        Osmotic_Permeate(j,i) = 0;
    end

    if ~(j==1 && i==1)
        Delta_Osmotic_Pressure(j,i) = Osmotic_Feed(ji)-
Osmotic_Permeate(j,i);
    end
```

```
    if ~(j==1)
        f(j,i) = 6.23/(RE(j-1,i))^0.3;
        Pressure_Feed(j,i) = Pressure_Feed(j-1,i) -
f(j,i)*Velocity_Feed(j-1,i)^2*RHO/L_C/2*Cell_Length;
    end

    if ~(i==1 || i==2)
        f_p(j,i) = 6.23/(RE(j,i-1))^0.3;
        Pressure_Permeate(j,i) = Pressure_Permeate(j,i-1) -
f_p(j,i)*Velocity_Permeate(j,i-1)^2*RHO/L_C/2*Cell_Length;
    end

    if ~(j==1 && i==1)
        Delta_P(j,i) = Pressure_Feed(j,i)-Pressure_Permeate(j,i);
        JV(j,i) = RP^2*(Delta_P(j,i)-
Delta_Osmotic_Pressure(j,i))/8/MU/DELTA;
    end

    if (i==1)
        JV(j,i) = RP^2*Delta_P(j,i)/8/MU/DELTA;
    end

    if ~(i==1)
        Flow_P(j,i) = Flow_P(j,i-1) + .5*(JV(j,i)+JV(j,i-1))*Contact_Surf;
        CP_Cell(j,:,i) = (Flow_P(j,i-1).*CP_Cell(j,:,i-1) + .5*CIP(j,:,i-
1)*(JV(j,i)+JV(j,i-1))*Contact_Surf)/Flow_P(j,i);
    end

    if ~(j==1 && i==1)
        Velocity_Permeate(j,i) = Flow_P(j,i)/Cross_AreaP;
    end

    if ~(j==1)
        Flow_B(j,i) = Flow_B(j-1,i) - .5*(JV(j,i)+JV(j-1,i))*Contact_Surf;
        CIB(j,:,i) = (Flow_B(j-1,i).*CIB(j-1,:,i) - .5*CIP(j-
1,:,i)*(JV(j,i)+JV(j-1,i))*Contact_Surf)/Flow_B(j,i);
```

```
        Velocity_Feed(j,i) = Flow_B(j,i)/Cross_AreaB;
    end

    Pe(j,:,i) = (1./D*2*Height_B*Velocity_Feed(j,i))';


%% Overall Paramaters

EMEMB = 40.4;                          %Dielectric Constant of Pore
EWATER = 80.4;                         %Dielectric Constant of Water
EPSX = 1;                              %Mesh Expansion Factor
F = 96500.0;                           %Faraday Constant [C/Eq]
ITMAX = 5000;                          %Max number of iterations
NCX = 100;                             %Max Number of Ions
NDX = 5000;                            %Max Number of Nodes
NV = (ND+1)*(NC+1);                    %Number of Variables
NVX = (NDX+1)*(NCX+1);                 %Max Number of variables
SMALL = 1e-15;                         %Small Value Parameter
TOL = 1.00e-4;                         %Maximum normalized Residual
URF = .2;                              %Under Relaxation Factor
KF = F/(R*T);                          %Ratio for better calculations [C/J]
NU = 8.97e-7;                          %Kinematic Viscosity of solvent
(water)
RE(j,i) = Velocity_Feed(j,i)*L_C/NU;        %Reynolds Number
RE_P(j,i) = Velocity_Permeate(j,i)*L_P/NU;  %Reynolds number of permeate



%% Ion data
Z = [1; -1];                       %Ionic Charge
RS = [1.84; 1.21]*1e-10;           %Ionic radii [m]
CX = -10.5;                          %Membrane Charge [mol/m^3]
CI0 = CIB(j,:,i);                  %Initialization of membrane concentration

%% Computation of Hindrance Factors and Steric Partition Coefficients
```

```
for IC=1:NC

    RL(IC) = RS(IC)/RP;                 %Ionic radius to pore radius ratio
    PHIL(IC) = (1-RL(IC))^2;            %Partition Factor due to Steric
Exclusion

    if (RL(IC)>=1.0)
        PHIL(IC) = SMALL;
        KDF(IC) = 1e-8;                 %Hindrance Factor for Diffusion
        KCV(IC) = 1e-8;                 %Hindrance Factor for Convection
    end

    if (RL(IC) <= .95)
        KDF(IC) = (1+ 9/8*RL(IC)*log(RL(IC)) -
1.56034*RL(IC)+.528155*RL(IC)^2 ...
                +1.91521*RL(IC)^3-2.81903*RL(IC)^4 + 0.270788*RL(IC)^5 +
...
                1.10115*RL(IC)^6 - 0.435933*RL(IC)^7)/(1-RL(IC))^2;
        KCV(IC) = (1+3.867*RL(IC)-1.907*RL(IC)^2-
.834*RL(IC)^3)/(1+1.867*RL(IC)-.741*RL(IC)^2);
    end

    if (.95 < RL(IC) && RL(IC) < 1.0)
        KDF(IC) = .984*((1-RL(IC))/RL(IC))^(2.5);
        KCV(IC) = (1+3.867*RL(IC)-1.907*RL(IC)^2-
.834*RL(IC)^3)/(1+1.867*RL(IC)-.741*RL(IC)^2);
    end

    DM(IC) = KDF(IC)*D(IC);             %Ion Diffusivity in the Membrane
Active layer[m^2/s]
    U(IC) = DM(IC)*KF;                  %Ion Mobility inside Membrane
[sqrt(C)/kg]



end
%% Mesh Generation
if (EPSX <= 1.0)
```

```
    EPSX = 1.0000001;
end
XM(ND) = DELTA;
XM(ND-1) = DELTA;
DX = DELTA/2/((1-EPSX^((ND-2)/2))/(1-EPSX));
for I=1:(ND-3)
    XM(ND-I-1)= XM(ND-I)-DX;
    DX = EPSX*DX;
end
XM(1) = 0;
for I = 1:(ND/2)
    XM(I)=DELTA-XM(ND-I);
    DX = EPSX*DX;
end

%% Mass Transfer Coefficient Correction, Steric and Dielectric Exclusion
for IC=1:NC

    DH(IC) =  6.95e-5*Z(IC)^2/RS(IC)*(1/EMEMB-1/EWATER);          %Born
solvation energy barrier [J]
    SC(IC) = NU/D(IC);                                             %Schmidt
number
    if (i==1 && j==1)
        Entry_Length(IC) = .05*L_C*SC(IC)*RE(j,i);
%Calculate Entry Length depending on first Reynolds number
    end
        KC(IC) =.753*(K/(2-K))^.5*D(IC)/Height_B*SC(IC)^(-
1/6)*(Pe(j,IC,i)*Height_B/L_mix)^(.5);
    if (KC(IC) == 0)
        KC(IC) = 10;
    end
    KPHI(IC) = JV(j,i)/KC(IC);                          %Temporary Variable
for  calculating KCDOT
    KCDOT(IC) = KC(IC)*(KPHI(IC)+ (1+.26*KPHI(IC)^1.4)^(-1.7));
%Corrected Mass Transfer Coefficient
    PHILE(IC) = exp(-DH(IC)/(R*T));
```

```
end


for I=1:ND              %Initialize Concentrations to feed concentration
in NCxND Matrix
    CI(:,I)= CIB(j,:,i);
end


PHI = zeros(1,ND);      %Initialize PHI to be all zeros
DPHIDX = 0;             %Initialize potential gradient at membrane surface
one feed side as zero.
A = zeros(NV);          %Initialize Matrix A
B = zeros(NV,1);        %Initialize Matrix B


%% Coefficient Assembly

for JITER = 1:ITMAX
%N-P Discretization Equations

IEQ = 0;
    for IC =1:NC
        for I=1:(ND-2)
            DX = XM(I+1)-XM(I);
            IEQ = IEQ+1;
            A(IEQ,(IC-1)*ND+I) = DM(IC)/DX + .5*JV(j,i)*KCV(IC) -
.5*Z(IC)*U(IC)*(PHI(I+1)-PHI(I))/DX;
            A(IEQ,(IC-1)*ND+I+1) = -DM(IC)/DX + .5*JV(j,i)*KCV(IC) -
.5*Z(IC)*U(IC)*(PHI(I+1)-PHI(I))/DX;
            A(IEQ, NC*ND+I) = .5*Z(IC)*U(IC)*(CI(IC,I+1)+CI(IC,I))/DX;
            A(IEQ, NC*ND+I+1) = -.5*Z(IC)*U(IC)*(CI(IC,I+1)+CI(IC,I))/DX;
            A(IEQ, IC*ND) = -JV(j,i);
            B(IEQ, 1) = -Z(IC)*U(IC)*.5*(CI(IC,I+1)+CI(IC,I))*(PHI(I+1)-
PHI(I))/DX;
```

```
        end
    end

%Charge Balance

    for I = 1:ND
        IEQ = IEQ+1;
        for IC = 1:NC
            A(IEQ, (IC-1)*ND+I) = Z(IC);      %for each ion, the charge is
also included in the overall A Matrix
        end
        if (I ~= ND)
            B(IEQ,1) = -CX;                   %the B Matrix holds the
overall membrane charge
        end
    end

%Feed-Membrane Equilibrium

    RIFB = 0;
    RIFM = 0;

    for IC = 1:NC
        RIFB = RIFB + 0.5*Z(IC)^2*CI0(IC)/1000;          %Ionic Strength
Parameters
        RIFM = RIFM + 0.5*Z(IC)^2*CI(IC,1)/1000;
    end
    ABULK = 1.825E6*(1/EWATER^3/T^3)^(.5);               %A parameter
equation 13
    AMEMB = 1.825E6*(1/EMEMB^3/T^3)^(.5);

%Activity Coefficients

    for IC = 1:NC
        IEQ = IEQ + 1;
        GAMAB = exp(-ABULK*Z(IC)^2*(RIFB^.5/(1+RIFB^.5)-0.3*RIFB));
        GAMABM = exp(-AMEMB*Z(IC)^2*(RIFM^.5/(1+RIFM^.5)-.3*RIFM));
```

```
        if (Z(IC) == 0)
            GAMAB = exp(.1*RIFB);
            GAMABM = exp(.1*RIFM);
        end
        GB(IC) = GAMAB/GAMABM;
        KE1 = PHIL(IC)*PHILE(IC)*GB(IC)*exp(-Z(IC)*KF*PHI(1));
        A(IEQ,(IC-1)*ND+1) = 1.0;
        A(IEQ, NC*ND+1) = CI0(IC)*Z(IC)*KF*KE1;
        B(IEQ,1) = CI0(IC)*KE1*(1+Z(IC)*KF*PHI(1));
    end
% Membrane- Permeate Equilibrium

    RIFB = 0;
    RIFM = 0;
    for IC = 1:NC
        RIFB = RIFB + .5*Z(IC)^2*CI(IC,ND)/1000;        %Ionic Strength
        RIFM = RIFM + .5*Z(IC)^2*CI(IC, ND-1)/1000;
    end

    for IC = 1:NC
        IEQ = IEQ+1;
        GAMAP = exp(-ABULK*Z(IC)^2*(RIFB^.5/(1+RIFB^.5)-.3*RIFB));
        if (Z(IC) ==0)
            GAMAP = exp(.1*RIFB);
        end
        GAMAPM = exp(-AMEMB*Z(IC)^2*(RIFM^.5/(1+RIFM^.5)-.3*RIFM));
        if (Z(IC) ==0)
            GAMAPM = exp(.1*RIFM);
        end

        GP(IC) = GAMAP/GAMAPM;                          %Ratio of
strengths
        KE2 = PHIL(IC)*PHILE(IC)*GP(IC)*exp(Z(IC)*KF*(PHI(ND)-PHI(ND-1)));
        A(IEQ, ND*IC-1) = 1/CI(IC,ND);
        A(IEQ, ND*IC) = -KE2/CI(IC,ND);
        A(IEQ, ND*(NC+1)-1) = Z(IC)*KF*KE2;
        A(IEQ,ND*(NC+1)) = -Z(IC)*KF*KE2;
```

```
        B(IEQ,1) = KE2*(-Z(IC)*KF*(PHI(ND)-PHI(ND-1)));

    end

%Feed Membrane Mass Transfer Resistance

    for IC = 1:NC
        IEQ = IEQ + 1;
        A(IEQ, ND*(NC+1)+IC) = KCDOT(IC) - JV(j,i);
        A(IEQ,IC*ND) = JV(j,i);
        A(IEQ, (ND+1)*(NC+1)) = Z(IC)*KF*D(IC)*CI0(IC);
        B(IEQ,1) = KCDOT(IC)*CIB(j,IC,i);
    end

%Feed Membrane Interface Charge Balance

    IEQ = IEQ + 1;

    for IC = 1:NC
        A(IEQ, ND*(NC+1)+IC) = Z(IC);
    end

    B = A\B;        %Matrix Solver
    x = B;



%Under Relaxation
    for I = 1:ND
        for IC = 1:NC
            DCI = (B((IC-1)*ND+I,1) - CI(IC,I))/(CI(IC,I));
            if (abs(DCI) > 1)
                DCI = abs(DCI)/DCI;
            end
            CI(IC,I) = CI(IC,I)*(1+URF*DCI);
        end
        PHI(I) = PHI(I)+ URF*(B(NC*ND+I,1)-PHI(I));
```

```
        if (abs(PHI(I))>5)
        PHI(I) = 0;
        end
    end

    for IC = 1:NC
        DCI = (B(ND*(NC+1)+IC,1)-CI0(IC))/CI0(IC);
        if(abs(DCI)>1)
            DCI = abs(DCI)/DCI;
        end
        CI0(IC)= CI0(IC)*(1+URF*DCI);
   end
    DPHIDX = DPHIDX+URF*(B((ND+1)*(NC+1),1) - DPHIDX);
    if (abs(DPHIDX)>500)
        DPHIDX= DPHIDX/abs(DPHIDX);
    end

%Re-Initializing Matrices
    A = zeros(NV);
    B = zeros(NV,1);

%%Residual Computations

    for IC = 1:NC
        RESCI(IC) = 0;
    end

    RESEQ = 0;
    RESBAL = 0;
    for I = 1:(ND-2)
        for IC = 1:NC
            DX = XM(I+1)-XM(I);
            RESCI(IC) = RESCI(IC)+ abs(-DM(IC)*(CI(IC,I+1)-CI(IC,I))/DX
...
                -.5*Z(IC)*U(IC)*(CI(IC,I+1)+CI(IC,I))*(PHI(I+1)-PHI(I))/DX
...
```

```
                +.5*JV(j,i)*KCV(IC)*(CI(IC,I+1)+CI(IC,I)) -
JV(j,i)*CI(IC,ND));
        end
        SUMC = 0;
        for IC = 1:NC
            SUMC = SUMC+ Z(IC)*CI(IC,I);
        end
        RESBAL = RESBAL+ abs(SUMC + CX); (HIGHLIGHTED)
    end

    for IC=1:NC
        if (PHIL(IC)<=SMALL)
            RESCI(IC) = 0;
        end
    end

    SUMC = 0;
    SUMCP = 0;
    SUMCTB = 0;
    for IC =1:NC
        SUMC = SUMC+Z(IC)*CI(IC,ND-1);
        SUMCP = SUMCP+Z(IC)*CI(IC,ND);
        SUMCTB = SUMCTB+abs(Z(IC)*CIB(j,IC,i));
    end
    RESBAL = RESBAL + abs(SUMC+CX)+abs(SUMCP);
    RESBAL = RESBAL/(SUMCTB +abs(CX));
    RJT = 0;
    for IC = 1:NC
        RJT =  RJT + abs(JV(j,i)*CI(IC,ND));
    end
    for IC = 1:NC
        RESCI(IC) = RESCI(IC)/RJT;      end

    %% Compute KC Residual
    if (KC(1) < 10)
        RESKC = 0;
        for IC = 1:NC
```

```
            RESKC = RESKC + abs(JV(j,i)*CI(IC,ND)+KCDOT(IC)*(CI0(IC)-
CIB(j,IC,i))+Z(IC)*KF*D(IC)*CI0(IC)*DPHIDX-JV(j,i)*CI0(IC))/RJT;
        end
    else
        RESKC = 0;
    end


    for IC = 1:NC
        if (PHIL(IC) > 1e-10)
            KE1 = PHIL(IC)*PHILE(IC)*GB(IC)*exp(-Z(IC)*KF*PHI(1));
            KE2 = PHIL(IC)*PHILE(IC)*GP(IC)*exp(-Z(IC)*KF*(PHI(ND-1)-
PHI(ND)));
            RESEQ = RESEQ + abs((CI(IC,1)/CI0(IC)/KE1)-1);

            if (CI(IC,ND) > 1e-11)
                RESEQ = RESEQ + abs((CI(IC,ND-1)/CI(IC,ND)/KE2)-1);
            end
        end
    end

    RM = 0;
    for IC = 1:NC
        if (RESCI(IC)>RM)
            RM = RESCI(IC);
        end
    end

    if (max([RM,RESBAL,RESKC, RESEQ]) < TOL)
        break
    end
end



for IC = 1:NC
```

```
    RREAL(IC) = (CI0(IC)-CI(IC,ND))/CI0(IC);
    ROBS(IC) = (CIB(j,IC,i)-CI(IC,ND))/CIB(j,IC,i);
end

CI0_list(j,:,i) = CI0(:);
ROBSERVED(j,:,i) = ROBS(:);
CIP(j,:,i) = CI(:,ND)';

end
end

RR = sum(Flow_P(:,end))/sum(Flow_B(1,:));

Power = 1/Eff*Flow_B(1)*(Pressure_Feed(1)-1e5);
```

THIS PAGE IS INTENTIONALLY LEFT BLANK

References

[1] I. D. A. (IDA), "IDA, Desalination Overview," [Online]. Available: http://idadesal.org/desalination-101/desalination-overview/.

[2] A. A. Hussain and A. E. Al-Rawajfeh, "Recent Patents of Nanofiltration Applications in Oil Processing, Desalination,Wastewater and Food Industries," *Recent Patents on Chemical Engineering,* vol. 2, pp. 51-66, 2009.

[3] "Webpage of the Royal Embassy of Saudi Arabia, Washington DC," [Online]. Available: http://www.saudiembassy.net/about/country-information/agriculture_water/Water_Resources.aspx.

[4] M. A. K. AI-Sofi, A. M. Hassan, G. M. Mustafa, A. G. I. Dalvi and M. N. M. Kither, "Nanofiltration as a means of achieving higher TBT of > 120°C in MSF," *Desalination,* vol. 118, pp. 123-129, 1998.

[5] W. R. Bowen and J. S. Welfoot, "Modelling of membrane nanofiltration—pore size distribution effects," *Chemical Engineering Science,* vol. 57, no. 8, p. 1393 – 1407, 2002.

[6] N. Hilal, H. Al-Zoub, N. A. Darwish, A. W. Mohammad and M. Abu Arabi, "A comprehensive review of nanofiltration membranes: Treatment, pretreatment, modelling, and atomic force microscopy," *Desalination,* vol. 170, pp. 281-308, 2004.

[7] W. R. Bowen and J. S. Welfoot, "Modelling the performance of membrane nanofiltration—critical assessment and model development," *Chemical Engineering Science,* vol. 57, p. 1121 – 1137, 2002.

[8] V. Geraldes and A. M. Brites Alves, "Computer program for simulation of mass transport in nanofiltration membranes," *Journal of Membrane Science,* vol. 321, p. 172–182, 2008.

[9] S. Bandini and D. Vezzani, "Nano¬filtration modeling: the role of dielectric exclusion in membrane characterization," *Chemical Engineering Science,* vol. 58, p. 3303 – 3326, 2003.

[10] R. Rautenbach and A. Groschl, "Separation Potential of Nanofiltration Membranes," *Desalination,* vol. 77, pp. 73-84, 1990.

[11] W. Jin, A. Toutianoush and B. Tieke, "Use of Polyelectrolyte Layer-by-Layer Assemblies as Nanofiltration and Reverse Osmosis Membranes," *Langmuir,* vol. 19, pp. 2550-2553, 2003.

[12] P. Eriksson, "Nanofiltration Extends the Range of Membrane Filtration," *Environmental Progress,* vol. 7, pp. 58-62, 1988.

[13] A. I. Schäfer, A. G. Fane and T. D. Waite, Nanofiltration : Principles and Applications, Oxford,UK; New York, NY: Elsevier, 2005.

[14] R. Rautenbach, K. Vossenkaul, T. Linn and T. Katz, "Waste water treatment by membrane processes - New development in ultrafiltration, nanofiltration and reverse osmosis," *Desalination,* vol. 108, pp. 247-253, 1996.

[15] W. R. Bowen and A. W. Mohammad, "Diafiltration by Nanofiltration: Prediction and Optimization," *AIChE Journal,* vol. 44, no. 8, pp. 1799-1812, 1998.

[16] A. E. Al-Rawajfeh, H. E. S. Fath and A. A. Mabrouk, "Integrated Salts Precipitation and Nano-Filtration as Pretreatment of Multistage Flash Desalination System," *Heat Transfer Engineering,* vol. 33, pp. 272-279, 2012.

[17] D. DeMichele, T. F. Seacord and P. J. Sutherland, "Manual of Practice for the Use of Computer Models for the Design of Reverse Osmosis/Nanofiltration Membrane Processes, Final Report," Texas Water Development Board, 2014.

[18] J. Schwinge, P. R. Neal, D. E. Wiley, D. F. Fletcher and A. G. Fane, "Spiral wound modules and spacers Review and analysis," *Journal of Membrane Science,* vol. 242, p. 129–153, 2004.

[19] W. R. Bowen and A. W. Mohammad, "Characterization and prediction of Nanofiltration membrane performance a General assessment," *Trans IChemE,* vol. 76, pp. 885-893, 1998.

[20] D. L. Oatley, L. Llenas, R. Pérez, P. M. Williams, X. Martínez-Lladó and M. Rovira, "Review of the dielectric properties of nanofiltration membranes and verification of the single oriented layer approximation," *Advances in Colloid and Interface Science,* vol. 173, p. 1–11, 2012.

[21] N. S. Kotrappanavar, A. A. Hussain, M. E. E. Abashar, I. S. Al-Mutaz, T. M. Aminabhavi and M. N. Nadagouda, "Prediction of physical properties of nanofiltration membranes for neutral and," *Desalination,* vol. 280, p. 174–182, 2011.

[22] N. Hilal, H. Al-Zoub, A. W. Mohammad and N. A. Darwish, "Nanofiltration of highly concentrated salt solutions up to seawater salinity," *Desalination,* vol. 184, p. 315–326, 2005.

[23] K. H. Mistry and J. H. Lienhard V, "Effect of nonideal solution behavior on desalination of a sodium chloride (NaCl)solution and comparison to seawater," *Journal of Energy Resources Technology,* vol. 135, 2013.

[24] K. H. Mistry, H. A. Hunter and J. H. Lienhard V, "Effect of composition and nonideal solution behavior on desalination calculations for mixed electrolyte solutions with comparison to seawater," *Desalination,* vol. 318, p. 34–47, 2013.

[25] M. A. K. Al-Sofi, "Fouling phenomena in multi stage flash (MSF) distillers," *Desalination,* vol. 126, pp. 61-76, 1999.

[26] O. A. Hamed, A. M. Hassan, K. Al-Shail and M. A. Farooque, "Performance analysis of a trihybrid NF/RO/MSF desalination plant," *Desalination and Water Treatment,* vol. 1, p. 215–222, 2009.

[27] C. O. Anne, D. Trebouet, P. Jaouen and F. Quemeneur, "Nanofiltration of seawater: fractionation of mono and multi-valent cations," *Desalination,* vol. 140, pp. 67-77, 2001.

[28] C. J. Harrison, Y. A. Le Gouellec, R. C. Cheng and A. E. Childress, "Bench-Scale Testing of Nanofiltration for Seawater Desalination," *J. Environ. Eng,* vol. 133, pp. 1004-1014, 2007.

[29] J. L. Andersen and J. A. Quinn, "Restricted Transport in Small Pores A Model for Steric Exclusion and Hindered Particle motion," *Biophysical Journal,* vol. 14, pp. 130-150, 1974.

[30] M. G. Davidsom and W. M. Deen, "Hydrodynamic Theory for the Hindered Transport of Flexible Macromolecules In Porous Membranes," *Journal of Membrane Science,* vol. 35, pp. 167-192, 1988.

[31] G. Schock and A. Miquel, "Mass transfer and pressure loss in spiral wound modules," *Desalination,* vol. 64, pp. 339-352, 1987.

[32] S. Senthilmurugan, A. Ahluwalia and S. K. Gupta, "Modeling of a spiral-wound module and estimation of model parameters using numerical techniques," *Desalination,* vol. 173, pp. 269-286, 2005.

[33] F. Evangelista, "An Improved Analytical Method for the Design of Spiral-wound modules," *The Chemical Engineering Journal,* vol. 38, p. 33 – 40, 1988.

[34] E. Nagy, E. Kulcsar and A. Nagy, "Membrane mass transport by nanofiltration: Coupled effect of the polarization and membrane layers," *Journal of Membrane Science,* vol. 368, p. 215–222, 2011.

[35] R. J. McCutcheon and M. Elimelech, "Influence of concentrative and dilutive internal concentration polarization on flux behavior in forward osmosis," *Journal of Membrane Science,* vol. 284, p. 237–247, 2006.

[36] R. Rautenbach and F. Helmus, "Some considerations on mass-transfer resistances in solution-diffusion-type membrane processes," *Journal of Membrane Science,* vol. 87, pp. 171-181, 1994.

[37] M. Dalwania, N. E. Benes, G. Bargeman, D. Stamatialis and M. Wessling, "Effect of pH on the performance of polyamide/polyacrylonitrile based thin film composite membranes," *Journal of Membrane Science,* vol. 372, p. 228–238, 2011.

[38] "Dow Water & Process Solutions FILMTEC™ Reverse Osmosis Membranes Technical Manual.".

[39] V. Geraldes, V. Semiao and M. N. de Pinho, "Flow management in nanofiltration spiral wound modules with ladder-type spacers," *Journal of Membrane Science,* vol. 203, p. 87–102, 2002.

[40] A. M. Hassan, M. Al-Sofi, A. M. Al-Ajlan, A. Al-Azzaz and A. Al-Mohammadi, "The New NF-SWRO Operation Increased Significantly UmmLujj SWRO Plant Output and Recovery".

[41] A. A. Al-Hajouri, A. S. Al-Amoudi and A. ,. M. Farooque, "Long term experience in the operation of nanofiltration pretreatment unit for seawater desalination at SWCC SWRO plant," *Desalination and Water Purification,* vol. 51, p. 1861–1873, 2013.

[42] C. Mazzoni, L. Bruni and S. Bandini, "Nanofiltration: Role of the Electrolyte and pH on Desal DK Performances," *Industrial & Engineering Chemistry Research,* vol. 46, pp. 2254-2262, 2007.